



## New trends in nanoparticle exsolution

Cite this: DOI: 10.1039/d4cc01983k

Alfonso J. Carrillo, \* Andrés López-García, Blanca Delgado-Galicia  and Jose M. Serra \*

Many relevant high-temperature chemical processes require the use of oxide-supported metallic nanocatalysts. The harsh conditions under which these processes operate can trigger catalyst degradation *via* nanoparticle sintering, carbon depositions or poisoning, among others. This primarily affects metallic nanoparticles created *via* deposition methods with low metal–support interaction. In this respect, nanoparticle exsolution has emerged as a promising method for fabricating oxide-supported nanocatalysts with high interaction between the metal and the oxide support. This is due to the mechanism involved in nanoparticle exsolution, which is based on the migration of metal cations in the oxide support to its surface, where they nucleate and grow as metallic nanoparticles partially embedded in the oxide. This anchorage confers high robustness against sintering or coking-related problems. For these reasons, exsolution has attracted great interest in the last few years. Multiple works have been devoted to proving the high catalytic stability of exsolved metallic nanoparticles in several applications for high-temperature energy storage and conversion. Additionally, considerable attention has been directed towards understanding the underlying mechanism of metallic nanoparticle exsolution. However, this growing field has not been limited to these types of studies and recent discoveries at the forefront of materials design have opened new research avenues. In this work, we define six new trends in nanoparticle exsolution, taking a tour through the most important advances that have been recently reported.

Received 25th April 2024,  
Accepted 10th June 2024

DOI: 10.1039/d4cc01983k

[rsc.li/chemcomm](https://rsc.li/chemcomm)

*Instituto de Tecnología Química, Universitat Politècnica de València, Consejo Superior de Investigaciones Científicas, 46022 Valencia, Spain. E-mail: [alcardel@itq.upv.es](mailto:alcardel@itq.upv.es), [jmserra@itq.upv.es](mailto:jmserra@itq.upv.es)*



**Alfonso J. Carrillo**

*Alfonso J. Carrillo holds a PhD in chemical engineering from Universidad Rey Juan Carlos (Spain) – research conducted at the IMDEA Energy Institute. Then, he moved to the Electrochemical Materials Laboratory, first at ETH Zurich (Switzerland), and later at MIT (USA), where he was a 2018 Eni-MIT Energy Fellow. He has been awarded with the Energy and Environmental Research Grant by Fundación Iberdrola, Juan de la Cierva Formación by the Spanish Ministry of Science, and Junior Leader Fellowship by Fundación LaCaixa. He has been working at ITQ (Spain) since January 2019, focusing on the functionalization of redox oxides for energy storage and the production of renewable fuels.*



**Andrés López-García**

*Andrés López-García obtained his BSc degree in chemistry and MSc degree in applied chemistry from Universidad Autónoma de Madrid. During this period, he was a research intern at ICMM and ICP institutes (both in Madrid, Spain) thanks to the scholarships granted by the Spanish Society of Catalysis (SECAT). In 2020, he joined ITQ (Valencia, Spain) to conduct his PhD studies, focusing on alloyed nanocatalyst exsolution for energy applications. He has recently received the Young Researcher Award 2023 by E-MRS (Strasbourg, France) and the Best Oral Presentation Award at the Autumn School on Inorganic Electrochemical Reactors (Valencia, Spain).*



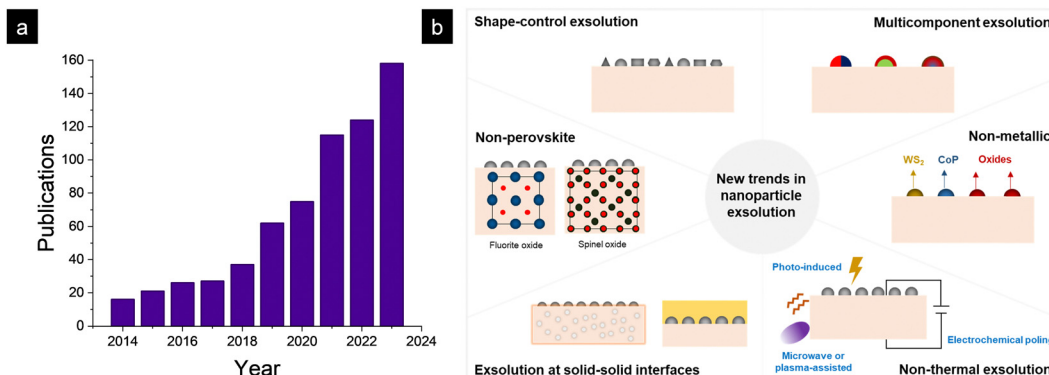


Fig. 1 (a) Evolution of publications on nanoparticle exsolution in the last decade. (b) The six new trends in nanoparticle exsolution that are covered in this article.

## Introduction

Oxide-supported metallic nanoparticles are at the core of a plethora of technologies, including traditional thermocatalytic processes for producing fuels and chemicals,<sup>1</sup> fuel cells and electrolyzers,<sup>2–4</sup> sensors<sup>5</sup> or even memory storage devices.<sup>6</sup> Specifically, in catalytic and electro-catalytic processes occurring at high temperatures (500–1000 °C), metallic nanoparticles can easily suffer from sintering-related phenomena if they are not firmly attached to the oxide support.<sup>7</sup> Eventually, metallic nanoparticle growth and agglomeration will increase the nanoparticle size and lower their dispersion over the oxide support, which will dramatically lower the catalyst activity. Thus, preventing nanoparticle sintering-related phenomena has been a major field of study in the catalysis and materials science communities to obtain robust and durable catalysts with enhanced lifetimes.<sup>8</sup> Based on this premise, in the last decade, nanoparticle exsolution has emerged as a promising alternative to conventional impregnation methods, allowing the

fabrication of highly resistant metallic nanoparticles.<sup>9</sup> This is mainly due to the mechanism through which exsolved nanoparticles grow.

Exsolution involves the migration of metallic cations contained in the crystal lattice of the bulk oxide, which, under reductive conditions, nucleate as nanoparticles on the oxide surface. The fact that the nanoparticles grow from the bulk rather than from a deposited precursor, as in impregnation, endows them with high resistance to sintering since the particles remain “anchored” to the oxide.<sup>10</sup> Additionally, the benefits of nanoparticle anchoring in preventing carbon deposition have been demonstrated.<sup>10</sup> These two beneficial properties of exsolved nanoparticles, among others, have prompted great interest in the scientific community, leading to exponential growth in the number of publications over the last decade<sup>1,11</sup> (Fig. 1a). However, it should be highlighted that pioneering works demonstrating nanoparticle exsolution were pointed out two decades ago, exemplified by the seminal article of Nishihata *et al.*<sup>12</sup> In this first decade, many contributions can



**Blanca Delgado-Galicia**

*Blanca Delgado-Galicia received her bachelor's degree in chemistry from Universidad Autónoma de Madrid. She continued her education at Universitat Politècnica de València where she pursued a Master's degree in Sustainable Chemistry. She obtained a scholarship from the Spanish Society of Catalysis (SECAT) to develop her Master Thesis, focused on the study of nanoparticle exsolution on ceramic materials. This project*

*was carried out at the Energy Conversion and Storage Group at the Instituto de Tecnología Química, where she is currently employed as a research assistant. Recently, she has received the USC-Genesal Energy award for the best Master Thesis on energy transition.*



**Jose M. Serra**

*Prof. José M. Serra completed his PhD at the Institute of Chemical Technology (ITQ) under the guidance of Prof. A. Corma, in collaboration with the Institute Français du Pétrole, followed by a 2-year postdoctoral stage at the Forschungszentrum Jülich, Germany. Since 2006 he has been the Head of the Energy Conversion and Storage group and, currently he is the Director of ITQ. For his contribution to the field, he has received the*

*ExxonMobil Chemical European Science and Engineering Award, Spanish Catalysis Society PhD Award, Christian Friedrich Schönbein Medal, European Ceramic Society Young Scientist Award, Medal of the Royal Spanish Engineering Academy and Air Liquide Scientific Prize.*



be found, especially on precious metal (Pd, Pt, and Ru) nanocatalyst exsolution from perovskite oxides.<sup>13–30</sup> Since then, many works have been devoted to mechanistic studies in which thermodynamics and kinetics of metallic nanoparticle exsolution have been assessed. These works lay the foundation for more efficient materials design, where a profound understanding of the physicochemical phenomena controlling exsolution is critical. In parallel, and according to the inherent emerging nature of this field, research efforts have also been put into expanding the limits of nanoparticle exsolution to new avenues, enlarging the materials design space of this novel nanocatalyst fabrication route.

## Background: how to control nanoparticle exsolution?

Besides its high robustness, one of the significant advantages of exsolution is its excellent capability for facile control over nanoparticle characteristics (morphological and compositional), which is an additional advantage of this fabrication method. This has attracted great interest in the community, which is focused on understanding the underlying mechanisms of this promising nano-fabrication method and finding structure–property relationships that could lead to more efficient catalysts or devices. Nanoparticle exsolution can be controlled by adjusting the external (conditions under which exsolution is performed) or internal factors (related to the oxide properties that serve as the host for nanoparticle exsolution). Regarding the former, parameters such as temperature, time and gas composition<sup>6,31–34</sup> have resulted in changes in nanoparticle size and dispersion. Longer exposure times and lower temperatures generally lead to larger nanoparticles and lower dispersions. These trends are directly related to the kinetics of nanoparticle nucleation and growth, which, under the aforementioned conditions, favour the latter. Longer exposure times have also been recently proven to alter the shape of exsolved nanoparticles.<sup>11</sup> The design of shape-controlled exsolved nanoparticles and their implications in the catalytic activity of heterogeneous reactions will be discussed in Section 1. It is important to emphasize here that morphological changes achieved *via* variations in the exsolution fabrication route should ensure an improvement in the catalytic (or device) performance while assuring long-term stability.

Additionally, changes in the conditions under which exsolution is performed can greatly impact the composition of the nanoparticles. A recent work illustrated that the exsolution temperature influences the composition of exsolved ternary alloy metallic nanoparticles.<sup>31</sup> The possibility of exsolving multiple B-site cations, leading to the formation of alloys or multi-elemental nanoparticles, is, undoubtedly, one of the main focuses of recent research in nanoparticle exsolution. Exsolved alloy nanocatalysts can unlock unprecedented catalytic properties, leading to higher activity while guaranteeing robustness over prolonged operation. The latest discoveries in

the conceptual design of multi-elemental (alloy) nanocatalysts will be covered in Section 2.

Time and temperature can be used to alter the composition of the exsolved nanoparticles, as well as the gas atmosphere. Traditionally, the exsolution field has focused on fabricating metallic nanoparticles. However, in many chemical reactions or physicochemical processes, other chemistries such as oxides, sulphides or phosphides are the active species. The exsolution field has not put aside the catalytic potential of these compounds, and lately, the exsolution of oxide<sup>35</sup> nanoparticles or sulphides<sup>36</sup> has been reported. Section 3 will analyze the recent advances in the design of non-metallic exsolved nanoparticles.

Temperature, time, and gas partial pressure are the external parameters commonly changed to control exsolution. A recent review by Ruh *et al.* has covered these aspects.<sup>11</sup> However, in recent years, metallic nanoparticle exsolution has been induced *via* non-thermal treatments such as electrochemical poling,<sup>37</sup> laser induction,<sup>38</sup> or applying plasma<sup>39</sup> or microwaves.<sup>40</sup> These methods have led to promising results in achieving higher exsolution extents or milder exsolution conditions in H<sub>2</sub>-free atmospheres, opening new avenues away from conventionally heating in reductive atmospheres. These latest trends will be discussed in Section 4.

Modifications in the material intrinsic (or internal) factors have also been widely studied in recent years to improve the exsolution capacity of oxide materials. One aspect that has greatly impacted the amount and shape of exsolved nanoparticles is oxide strain. Strain engineering has been mainly studied in thin films due to the relative ease with which strain can be induced in a thin film oxide by a lattice mismatch with the support in which it is deposited.<sup>41</sup> Namely, for La<sub>0.2</sub>Sr<sub>0.7</sub>Ni<sub>0.1</sub>Ti<sub>0.9</sub>O<sub>3–δ</sub>, compressive strain was found to increase the exsolved nanoparticle population, leading to the exsolution of smaller nanoparticles compared to tensile strain.<sup>41</sup> Interestingly, the relationship between strain and nanoparticle exsolution can be reverse-engineered as it has been recently demonstrated in bulk oxides.<sup>42–44</sup> Here, exsolution is explicitly aimed at forming endogenous nanoparticles that precipitate inside the oxide bulk together with conventional surface exsolution. These metallic precipitates induce tensile strain in the perovskite oxide, which significantly enhances the oxygen exchange capacity of these materials, a fundamental property in the chemical looping production of syngas.<sup>43</sup> The design of oxides functionalized with endogenous nanoparticles will be covered in Section 5.

The influence of the plane direction on nanoparticle exsolution has been explored using thin film exsolution. Kim *et al.* discovered that nanoparticle population and shape strongly correlate with the plane orientation in perovskite titanates.<sup>45</sup> In particular, the (111) plane led to higher populations, whereas the (001) plane led to larger, more elongated particles.<sup>45</sup> Here, the authors demonstrated the relevance of interfacial energies in the shape and dispersion of exsolved nanoparticles.

A-site deficiency has been conventionally employed as a compositional modification to enhance the number of exsolved nanoparticles.<sup>46</sup> In a recent work, O'Leary and co-authors shed



more light on the influence of A-site deficiency and composition on the energetics of Ni nanoparticle exsolution from perovskite titanates.<sup>47</sup> However, in some cases, A-site deficiency is not favourable since it can lead to compositional instabilities, eventually resulting in the segregation of transition metal oxides such as NiO in non-stoichiometric double perovskites.<sup>31</sup> This affects the extent of exsolution since not all the exsolvable B-site cations are in the perovskite oxide crystal lattice, causing a decrease in the nanoparticle surface dispersion compared to stoichiometric materials. Our group recently found that by partially replacing Sr in the A-site with trivalent lanthanides, it was possible to reduce the amount of NiO segregations in  $\text{Sr}_{1.9}\text{Fe}_{1.3}\text{Ni}_{0.2}\text{Mo}_{0.5}\text{O}_{6-\delta}$  double perovskites.<sup>48</sup> We also found that there was a correlation between the lattice parameters induced by this lanthanide-doping strategy and the extent of exsolution, in which incorporation of larger cations, e.g.,  $\text{La}^{3+}$  resulted in a decrease of the exsolved nanoparticle population.<sup>48</sup> These results emphasize how alterations in material properties can directly affect the exsolution behavior of the perovskite family.

Finally, in the last section, we will assess the recent progress on metallic nanoparticle exsolution from non-perovskite oxide materials (Section 6). This is quite a relevant topic since it can expand the realm of exsolution to other oxides conventionally used as supports in catalysis, such as fluorites, e.g., ceria or zirconia. In a recent work, we demonstrated that Ru exsolution from  $\text{CeO}_2$  significantly boosted the chemical looping performance of this type of materials for syngas production *via* methane partial oxidation.<sup>49</sup> Exsolution from other oxides such as yttria-stabilized zirconia, pyrochlores and spinels will also be covered in this section, emphasizing the main differences that arise when comparing with perovskite exsolution.

This Feature Article presents a brief but thorough analysis of six trends in nanoparticle (Fig. 1b) exsolution based on the latest discoveries in this emerging field, emphasizing the discoveries led by ITQ. This work aims to connect these recent findings with future directions that will help designing durable materials with high catalytic activity by applying the exsolution method, regardless of the application or end-use of these catalysts. Specific applications and detailed thermodynamic or kinetic aspects will not be covered here, although their importance is key for more efficient exsolution design.

## New trends in nanoparticle exsolution

### 1. Shape-control exsolved nanoparticles

Most exsolution studies focus on the size or population of nanoparticles as these are straightforward factors to control. These are usually modified by changing the temperature (or time) of reduction. For instance, increasing the temperature leads to an increase in the size of the nanoparticles while reducing their dispersion. Besides these morphological properties, modifying other characteristics of the exsolved nanoparticles would also be interesting, like the acquired shape during exsolution. This can, indeed, be modified by adjusting

the process conditions and may significantly impact the catalytic performance of these nanoparticles. For example, for polyhedral-shaped nanoparticles, the exposed surface is higher than that of spherical ones for the same volume.<sup>50</sup>

Conventionally, exsolution of metallic species tends to generate spherical-shaped nanoparticles. However, several works report alternative shapes, even demonstrating strategies to control the geometry of the exsolved metallic nanoparticles. To date, and the best of our knowledge, only two reports show how changing exsolution parameters can tune the exsolved nanoparticle's shape. The first of these two studies, by Neagu *et al.*,<sup>51</sup> Fig. 2a–d, demonstrates how the exsolution gas atmosphere plays an important role in shaping the emerging nanoparticles. Usually, as previously mentioned, spherical-shaped nanoparticles are expected when exsolving metallic species, like Ni from  $\text{La}_{0.8}\text{Ce}_{0.1}\text{Ni}_{0.4}\text{Ti}_{0.6}\text{O}_{3-\delta}$ , as shown in Fig. 2b after 650 °C, 10 hours under  $\text{H}_2$  flow reduction treatment. However, cubic-shaped nanoparticles were formed when this same material was subjected to 5% CO at 900 °C for 10 h (Fig. 2c). Remarkably, applying humidified (2.5%  $\text{H}_2\text{O}$ ) 5%  $\text{H}_2$  flow at 1000 °C for 10 h generated ellipsoidal-shaped nanoparticles interfaced with  $\text{La}_2\text{TiO}_5$  oxide (Fig. 2d). In this same work, even vacuum conditions were explored for exsolution. From  $\text{La}_{0.43}\text{Ca}_{0.37}\text{Ni}_{0.03}\text{Ti}_{0.94}\text{O}_{3-\delta}$  perovskite, strongly faceted nanoparticles emerged upon heating up to 900 °C under vacuum (Fig. 2a). These results show the high impact that the exsolution treatment gas atmosphere and/or pressure can have on the shape of the exsolved nanoparticles, in this case, Ni.

Kim *et al.* also conducted their work on Ni-doped lanthanum titanate, reporting shape alterations with temperature variation.<sup>50</sup>  $\text{La}_{0.7}\text{Ca}_{0.2}\text{Ni}_{0.25}\text{Ti}_{0.75}\text{O}_{3-\delta}$  under a dry  $\text{H}_2$  atmosphere at temperatures ranging from 600–800 °C, either for short durations (3 h) or longer ones (24 h), resulted in the exsolution of spherical-shaped nanoparticles (Fig. 2e). But, when the temperature was raised up to 1000 °C, faceted nanoparticles were obtained, Fig. 2f and g. They proved the importance of exploring different nanoparticle shapes since the faceted Ni nanoparticles exhibited a longer and higher conversion of  $\text{CH}_4$  in dry reforming of methane reaction compared to spherical-shaped and infiltrated Ni catalysts.<sup>50</sup>

As previously mentioned, there are some other studies where non-spherical shaped nanoparticles are exsolved without reporting control over their shape. For instance, Fe-based nanorod formation was observed when  $\text{La}_{0.6}\text{Sr}_{0.4}\text{FeO}_{3-\delta}$  was exposed to  $\text{H}_2$  at 600 °C.<sup>52</sup> For the same composition, flattened particles emerged when subjected to a 3%  $\text{H}_2$  (650 °C, 5 h) treatment,<sup>53</sup> proving how the atmosphere plays, indeed, a relevant role modify specific morphological properties of the exsolved nanoparticles.

Finally, since exsolution can potentially be reverted under oxidizing conditions, partial or complete redissolution of the exsolved nanoparticles is expected under certain adequate conditions. For instance, one of the requirements for exsolved NP re-dissolution is that the perovskite is A-site stoichiometric.<sup>12,14,16,54</sup> However, Neagu *et al.* published some interesting results involving morphological changes affecting Ni and



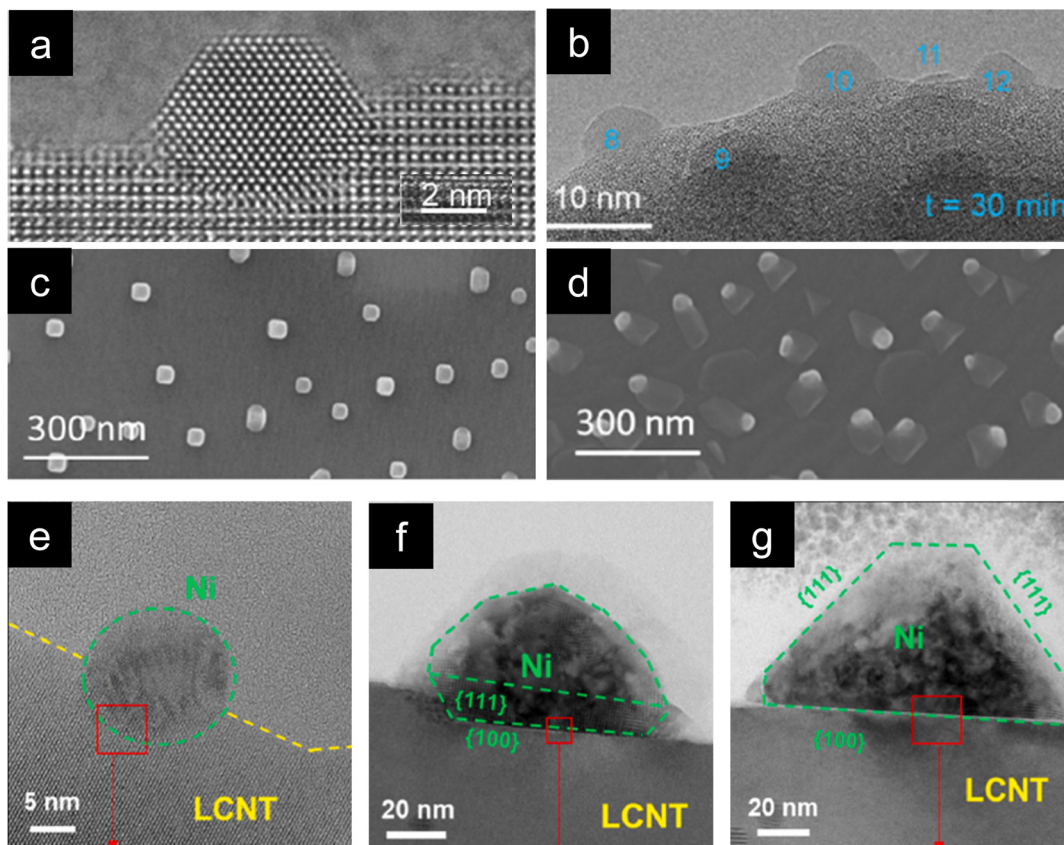


**Fig. 2** (a) ETEM micrographs of  $\text{La}_{0.43}\text{Ca}_{0.37}\text{Ni}_{0.03}\text{Ti}_{0.94}\text{O}_{3-\delta}$  faceted exsolved nanoparticle generated in vacuum at  $900\text{ }^\circ\text{C}$ . (b)–(d) ETEM micrographs of  $\text{La}_{0.8}\text{Ce}_{0.1}\text{Ni}_{0.4}\text{Ti}_{0.6}\text{O}_{3-\delta}$  exsolution: (b) spherical-shaped nanoparticles ( $\text{H}_2$ ,  $650\text{ }^\circ\text{C}$ ); (c) cubic-shaped nanoparticles (5%  $\text{CO}$ ,  $900\text{ }^\circ\text{C}$ , 10 h); (d) ellipsoidal-shaped nanoparticles (2.5%  $\text{H}_2\text{O}/5\%\text{ H}_2$ ,  $1000\text{ }^\circ\text{C}$ , 10 h). Reprinted (adapted) with permission from D. Neagu, V. Kyriakou, I. Roiban, M. Aouine, C. Tang, A. Caravaca, K. Kousi, I. Schreur-Piet, I. S. Metcalfe, P. Vernoux, M. C. M. van de Sanden and M. N. Tsampas, *ACS Nano*, 2019, **13**, 12996–13005. Copyright 2019 American Chemical Society. High-voltage transmission electron microscopy micrographs showing the evolution with time and temperature of Ni nanoparticles from  $\text{La}_{0.7}\text{Ca}_{0.2}\text{Ni}_{0.25}\text{Ti}_{0.75}\text{O}_{3-\delta}$  under a  $\text{H}_2$  gas flow: (e)  $800\text{ }^\circ\text{C}$ , 24 h; (f)  $900\text{ }^\circ\text{C}$ , 3 h; and (g)  $900\text{ }^\circ\text{C}$  24 h. Reproduced with permission from ref. 50.

Co-Ni exsolved nanoparticles when subjected to a  $\text{CO} + \text{O}_2$  flow for carbon monoxide combustion. Under these conditions, more faceted shapes were first obtained, which led to cubic  $(\text{Co,Ni})_3\text{O}_4$  spinels instead of redissolution.<sup>55</sup>

## 2. Multi-elemental metallic nanoparticle exsolution

One fascinating aspect of metallic exsolution relies on the possibility of simultaneously exsolving several species and, thereby, creating multi-elemental nanoparticles in a relatively facile manner. This is mainly due to the easy compositional tunability of perovskite oxides, facilitating the incorporation of a wide variety of cations in both the A and B sites of the  $\text{ABO}_3$  perovskite structure. Specifically, the target has been to combine several cations with adequate thermodynamic properties for exsolution from the B-site. Here, it should be kept in mind that some metals, namely, Ag, usually occupy the A-site and have been shown to generate nanoparticles upon exsolution, although to date,<sup>56,57</sup> metallic multi-elemental exsolution has mainly focused on metals located at the B-site of the perovskite. In this context, as mentioned earlier, it is crucial to properly select metals for partial B-site substitution, as not every

element is thermodynamically favored to exsolve. This matter has already been studied by Carrillo *et al.*, showing the thermodynamic tendency for reduction (and, thereby, for exsolution) *via* calculations of Gibbs free energy ( $\Delta G$ ) for several metallic species.<sup>58</sup> These studies reveal that metallic cations such as Ni, Fe, Co or several noble metals (Ru, Rh, Pt...) are thermodynamically favored for exsolution ( $\Delta G < 0$ ). In contrast, Mn, Ti or Mg are not expected to exsolve as metals. Therefore, accurate materials design *via* partial substitution of B-site atoms with exsolvable species can lead to a multicomponent exsolution process. Mainly, this phenomenon has been studied for bimetallic alloy exsolution, but in the past few years multi-elemental exsolution has experimented a remarkable development, aiming not only to achieve more complex alloys, but also to reveal the possibility of generating non-alloyed multicomponent nanoparticles.

**a. Binary alloys.** The exsolution of several metallic cations has been of great interest in producing a wide range of alternative functionalized materials. Combining different elements into alloyed metallic nanoparticles offers the possibility of generating nanocatalysts with altered properties compared to



single metal ones, which may significantly impact their applications or stability.

The exsolution of multicomponent nanoparticles has usually been related to binary alloys, and nowadays a major part of the published studies deals with this matter. In fact review articles about bimetallic alloy exsolution have already been published. For instance, the study by Tang *et al.* not only explores different exsolvable alloys (mainly concerning Fe, Co and Ni), but also investigates the mechanisms behind this process.<sup>59</sup> Previous DFT studies performed by Kwon *et al.* focusing on Ni–Co alloy exsolution suggested that the most thermodynamically favored pathway for alloyed nanoparticle exsolution relies on the independent co-segregation to the surface of each metal together with oxygen vacancies ( $V_{\text{O}}^{\bullet\bullet}$ ). Later, aggregation of Ni and Co species results in the formation of alloyed nanoparticles. This surface alloy formation (Fig. 3a) would be preferential over the bulk alloy formation, followed by segregation to the surface, according to the Gibbs energies calculated in this work.<sup>60</sup>

In this context, a wide variety of bimetallic alloys have been exsolved from a diverse range of materials, including not only perovskites ( $\text{ABO}_3$ ) and double perovskites ( $\text{A}_2\text{B}_2\text{O}_6$ ), but also other structures, like fluorite-based structures, (*i.e.*,  $\text{CeO}_2$ ). The following sections will further discuss this matter in depth (see Section 6). Since bimetallic exsolution has already been widely explored by other authors, and this work focuses on the most recent trends in nanoparticle exsolution, this subsection will not delve into deep detail. However, it is essential to highlight the wide variety of applications in which bimetallic exsolution proved to be useful. For instance, Fe–Ni alloyed exsolved nanoparticles proved to perform better than non-alloyed Ni nanoparticles in CO oxidation reactions.<sup>63</sup> Fe–Ni alloys have also been exsolved from perovskites to significantly improve the catalytic activity of  $(\text{La}_{0.75}\text{Sr}_{0.25})(\text{Cr}_{0.5}\text{Fe}_{0.5-x}\text{Ni}_x)\text{O}_3$  perovskites for methane reforming reaction.<sup>64</sup> In fact, Fe–Ni alloyed nanoparticles (which generally form  $\text{FeNi}_3$  compositions) have been commonly explored as promising candidates for dry reforming of methane.<sup>65,66</sup> In particular, our group found that increasing the Ni/Fe ratio on the B-site of  $\text{Sr}_2\text{Fe}_{1-x}\text{Ni}_x\text{MoO}_{6-\delta}$  double perovskites enabled a greater extent of nanoparticle exsolution, which eventually increased  $\text{CO}_2$  and  $\text{CH}_4$  conversion.<sup>65</sup> This result corroborates that Ni exhibits more favorable thermodynamics and kinetics for metal nanoparticle exsolution. Fe–Ni alloy exsolution also has a great interest in electrocatalysis applications, especially in solid oxide cells (SOCs).<sup>67–71</sup>

Other bimetallic alloys have proved to be versatile for applications, like FeCo exsolved nanoparticles. Just as in the FeNi case, materials functionalized with FeCo bimetallic exsolution exhibited enhanced catalytic activity in several applications, like in  $\text{PrBaFeCoO}_{5+\delta}$  double perovskite for dry reforming of methane.<sup>72</sup> FeCo exsolution has also been employed successfully in solid oxide fuel cells (SOFCs),<sup>73</sup> proton-conducting fuel cells (PCFC)<sup>74,75</sup> or in double perovskite cathodes for  $\text{CO}_2$  electrolysis in solid oxide electrolytic cells (SOECs).<sup>76</sup> This last work reported remarkable results regarding the possibility of redissolving FeCo alloyed exsolved nanoparticles from

Co-doped  $\text{Sr}_2\text{Fe}_{1.5}\text{Mo}_{0.5}\text{O}_{6-\delta}$ , extending the possibility of reversible exsolution to alloyed nanoparticles.

Most recently, alternative alloys involving noble metals have also been explored, mainly with Ru. Based on the same  $\text{Sr}_2\text{Fe}_{1.5}\text{Mo}_{0.5}\text{O}_{6-\delta}$  double perovskite structure, Lv *et al.* obtained FeRu alloyed nanoparticles to functionalize  $\text{CO}_2$  electrolysis fuel electrodes.<sup>77</sup> Nevertheless, the most remarkable result in this work was the demonstration of the promotion of exsolution through repeated redox manipulations. This work proved an increase in the extent of exsolution after several reduction–oxidation cycles using *in-situ* STEM. In addition, FeRu alloy exsolution caused a notable improvement in the SOEC performance. Guo *et al.* also obtained alloyed nanoparticles from double perovskites, namely, NiRu alloys from A-site deficient  $\text{La}_{2-x}\text{NiRuO}_{6-\delta}$  for their application in symmetrical cells. Interestingly, this work showed the lowest thermal exsolution temperature achieved to date (350–450 °C).<sup>78</sup>

**b. Ternary alloys.** Despite the notable growth experienced by binary alloy exsolution over the past few years, the development of more complex alloys is still limited. The possibility of combining more than two metals in exsolved nanoparticles would bring new properties to the functionalized materials, which can enhance the performance of the catalysts. More complex alloys can, thereby, open a new path for an appropriate and thorough design of the catalysts according to the needs of the desired reaction or process. For instance, Joo *et al.* studied the performance of different single metals and alloys for dry methane reforming.<sup>79</sup> They proved increased catalytic activity of FeCoNi exsolved nanoparticles from double perovskites compared to single metal (Fe and Ni) and bimetallic alloys (NiCo).<sup>79</sup> With DFT calculations, variations were observed in  $\text{CH}_4$  conversion rates due to electronic differences between alloys and single metals, affecting the d-band centers. So then, more complex alloys can, indeed, outperform binary exsolved alloys for specific processes. These FeCoNi ternary alloys were obtained *via* topotactic exsolution. In this case, only Co and Ni were exsolved from the perovskite lattice, not all three. Fe was incorporated by infiltrating the surface with a solution of an iron precursor, which, after a thermal treatment, reacted with CoNi exsolved nanoparticles, forming ternary alloys.

Besides this work, limited publications concerning the exsolution of ternary alloys have been published. Maybe the first direct exsolution of a ternary alloy was achieved by Santaya *et al.*, who were able to exsolve ternary FeCoNi nanoparticles at 700 °C and 10% wet  $\text{H}_2$  in an Ar atmosphere from  $\text{Sr}_{0.93}(\text{Ti}_{0.3}\text{Fe}_{0.56}\text{Ni}_{0.07}\text{Co}_{0.07})\text{O}_{3-\delta}$  perovskites.<sup>80</sup> These functionalized materials were tested as electrodes in symmetrical SOFCs, exhibiting a significant improvement in their performance after exsolution, indicating an enhancement in electrocatalytic activity. Most recently, another work has reported exsolution of FeCoNi from  $\text{Sr}_{0.9}\text{Co}_{0.5}\text{Fe}_{0.35}\text{Ni}_{0.15}\text{O}_{3-\delta}$  to improve the electrocatalytic performance for oxygen evolution reaction (OER), with satisfactory results.<sup>81</sup>

In this context, in our previous work, we wanted to achieve direct ternary alloyed nanoparticles from a double perovskite system based on  $\text{Sr}_2\text{Fe}_{1.5}\text{Mo}_{0.5}\text{O}_{6-\delta}$ .<sup>31</sup> The physicochemical



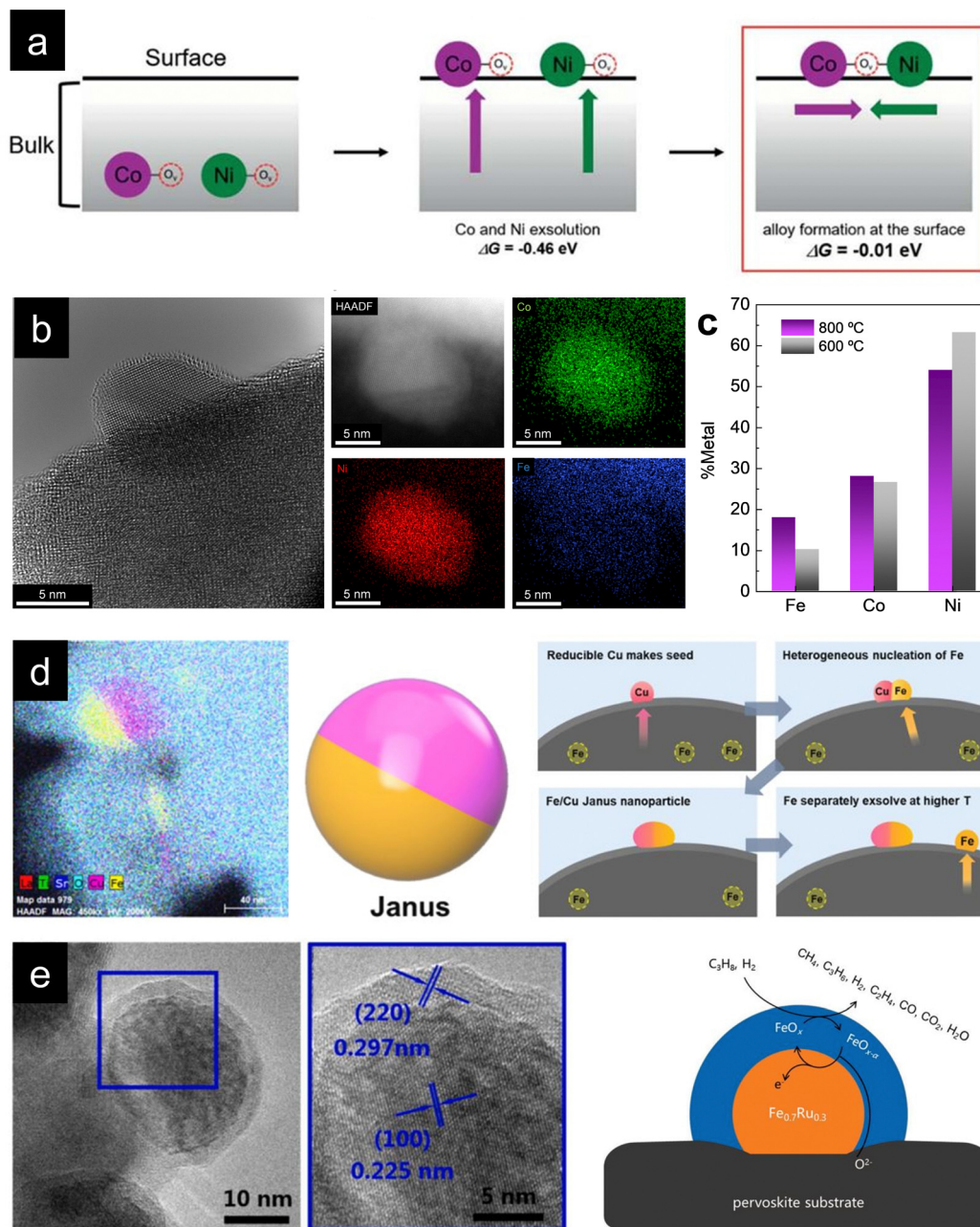


**Fig. 3** (a) Thermodynamically favored mechanism for alloy exsolution. Co-segregation of each metal together with oxygen vacancies ( $V_{O}^{\bullet\bullet}$ ) followed by superficial aggregation of metallic species (surface alloy formation) is preferential over bulk alloy formation. Reproduced with permission from ref. 60 with permission from the Royal Society of Chemistry. (b) High-resolution TEM and HAADF-STEM images, including EDXS mapping analyses, of ternary-alloyed exsolved FeCoNi nanoparticles from  $Sr_2FeCo_{0.2}Ni_{0.2}Mn_{0.1}Mo_{0.5}O_{6-\delta}$  at 600 °C, 4 h, and a 5%  $H_2/Ar$  atmosphere. (c) Compositional comparison of FeCoNi ternary alloys exsolved for 4 h, in a 5%  $H_2/Ar$  atmosphere, at 600 and 800 °C. Exsolution temperature proved to be crucial for tuning the metallic rates in the generated alloyed nanoparticles. (d) Multi-elemental non-alloyed Fe-Cu exsolution of Janus type nanoparticles and co-segregation mechanism from  $La_{0.43}Sr_{0.37}Fe_{0.09}Cu_{0.03}Ti_{0.88}O_{3-\delta}$  exsolution. Adapted with permission from ref. 61. (e) Multi-elemental exsolution of core-shell nanoparticles, consisting of a metallic  $Fe_{0.7}Ru_{0.3}$  core and a  $FeO_x$  shell. This structure has a key role in the reaction mechanism when employing these functionalized  $(Pr_{0.5}Sr_{0.5})_{0.9}Fe_{0.8}Ru_{0.1}Nb_{0.1}O_{3-\delta}$  perovskite materials as anodes in an  $H_2$  or  $C_3H_8$  SOFC. Adapted with permission from ref. 62.

properties of this family of materials make them exciting candidates for their use as electrodes for both SOEC<sup>82</sup> and SOFC<sup>83</sup> technologies or even symmetrical cells.<sup>84</sup> As discussed in the binary alloy subsection, B-site partial substitution of Fe with other elements has already led to the direct exsolution of alloyed nanoparticles, for instance, FeCo, FeNi or FeRu.

Moreover, B-site substitution of Fe with non-exsolvable elements, like Mn, demonstrated the possibility of improving specific properties of these materials, as Jiang *et al.* showed that in their work with  $Sr_2Fe_{1.4}Mn_{0.1}Mo_{0.5}O_{6-\delta}$  double perovskites.<sup>82</sup> For all these reasons, we developed  $Sr_2FeCo_{0.2}Ni_{0.2}Mn_{0.1}Mo_{0.5}O_{6-\delta}$  fuel electrodes for  $CO_2$  electrolysis in SOEC devices.<sup>31</sup>



With this material, FeCoNi exsolution was achieved (Fig. 3b) for the first time in this kind of double perovskites at different treatment temperatures (600, 700 and 800 °C) to investigate morphological changes of the nanoparticles with variations in external parameters. Lower exsolution temperatures led to higher population rates and smaller nanoparticles, namely, 1800, 1200 and 550  $\mu\text{m}^{-2}$  (dispersion) and 8.9, 11.6 and 21.3 nm (mean sizes) at 600, 700 and 800 °C, respectively. These results showed that the morphological properties of the exsolved nanoparticles can be tuned by changing external treatment parameters, in this case, temperature. However, during this research, we wanted to achieve more profound control over the exsolution of ternary alloys, more specifically, over the composition of the exsolved alloyed nanoparticles. For this purpose, compositional analyses of the obtained nanoparticles *via* EDXS were carried out, comparing the generated nanoparticles at 600 and 800 °C. The question was if, besides morphological properties, the composition of the alloys could also be controlled and tuned by changing the exsolution treatment parameters, focusing on the applied temperature. Santaya *et al.* showed that the nanoparticles contained similar amounts of the three metals, whereas in our case, Ni is the main component of the alloy for both 600 and 800 °C exsolutions, followed by Co and Fe (Fig. 3c). Nevertheless, interesting changes can be observed with temperature variation during exsolution since Fe content experienced a twofold increase at 800 °C compared to the 600 °C treatment. Co amounts remain relatively unaltered, while Ni amount decreases after 600 °C reduction. These results proved, for the first time to our knowledge, that in addition to morphology, the composition of exsolved alloyed nanoparticles can be easily modified by adjusting external parameters of the reduction treatment, which can lead to a more rational and efficient design of catalysts *via in-situ* exsolution.

**c. More complex alloys.** Considering the continued underdevelopment of ternary alloys, obtaining more complex alloys *via* exsolution remains almost unexplored. In fact, the only report to date was the one by Hou *et al.*, in which reduction at 400 °C under  $\text{H}_2$  of a high-entropy oxide  $\text{Zr}_{0.5}(\text{NiFeCuMnCo})_{0.5}\text{O}_x$  resulted in CoFeCuNi alloyed nanoparticles exsolution (around 30 nm).<sup>85</sup> Additionally, and in line with previously mentioned research, reversible exsolution of these alloyed nanoparticles after  $\text{H}_2$ /Air cycles is reported. These functionalized materials exhibited a remarkable catalytic behavior, specifically in long-term reverse water gas shift (RWGS) tests at 400 °C (500 h in continuous  $\text{CO}_2$  hydrogenation). More complex compositions such as NiFeCoCuPd have been the focus of the work of Gilliard-AbdulAziz and co-authors as recently reviewed in ref. 86.

**d. Multi-elemental non-alloyed exsolution.** While most publications concerning multi-elemental exsolution report alloys, several works claim the formation of alternative multi-elemental non-alloyed structures during the exsolution of various metallic species. For instance, Jo *et al.* studied the bimetallic exsolution of Cu and Fe from  $\text{La}_{0.43}\text{Sr}_{0.37}\text{Fe}_{0.09}\text{Cu}_{0.03}\text{Ti}_{0.88}\text{O}_{3-\delta}$  perovskites to use them as electrodes in reversible

SOCs.<sup>61</sup> Contrary to the expected FeCu alloy after exsolution, Fe–Cu Janus nanoparticles were obtained with 800 °C reduction treatment (12 h under  $\text{H}_2$  flow). As it can be seen in Fig. 3d, a phase-separated Fe–Cu heterostructure forms during the exsolution treatment. These Janus heterostructures presented a remarkable electrocatalytic performance for  $\text{H}_2\text{O}$  and  $\text{CO}_2$  electrolysis, achieving 1.1  $\text{A cm}^{-2}$  at 900 °C and 1.3 V. In addition, this work proved the triggering effect of Cu exsolution on Fe segregation and subsequent formation of multicomponent nanoparticles. As already explored and compiled in the review article by Tang *et al.*, the low segregation energy of Fe cations hinders its exsolution.<sup>59</sup> In fact, metallic Fe exsolution is not observed in some perovskite systems in which Fe is the only exsolvable cation in B-site positions. For instance, for  $\text{Sr}_2\text{Fe}_{1-x}\text{Ni}_x\text{MoO}_{6-\delta}$  double perovskites, incorporation of Ni was required to achieve metallic exsolution, whereas a material without Ni incorporation did not show any exsolution.<sup>65</sup> However, Fe exsolution has been reported for other perovskite systems, namely  $\text{La}_{0.6}\text{Sr}_{0.4}\text{FeO}_{3-\delta}$  or  $\text{SrFe}_{0.3}\text{Ti}_{0.7}\text{O}_{3-\delta}$ , by applying cathodic bias,<sup>87</sup> or in  $\text{Sr}_2\text{Fe}_{1+x}\text{Mo}_{0.5}\text{O}_{6-\delta}$  by increasing the stoichiometric ratio of Fe.<sup>88</sup> Nevertheless, as the mechanism in Fig. 3d explains, Cu reduction (and, thus, exsolution) would act like a nucleation seed, stimulating the subsequent exsolution of Fe and, thereby, resulting in the formation of Fe–Cu Janus-type nanoparticles. Fe would only exsolve separately at higher treatment temperatures.

Other alternative multi-elemental nanoparticles exsolved are core–shell structures. Several works deal with this matter, such as Qin *et al.* publication, in which exsolved  $(\text{Pr}_{0.5}\text{Sr}_{0.5})_{0.9}\text{Fe}_{0.8}\text{Ru}_{0.1}\text{Nb}_{0.1}\text{O}_{3-\delta}$  perovskite was employed as an electrocatalyst for SOFC anodes.<sup>62</sup> After 900 °C and 2 h under wet  $\text{H}_2$  treatment (about 50 nm of mean size), the exsolved nanoparticles exhibited a clear core–shell structure, as seen in Fig. 3e. This core consisted of a FeRu alloy (70 : 30 molar ratio) and a thinner shell of Fe oxides ( $\text{FeO}_x$ ). This core–shell structure seems to be crucial for explaining the reaction process, and the authors proposed a reaction mechanism involving both the core and shell of the exsolved nanoparticles, exhibiting promising electrocatalytic results when using wet  $\text{H}_2$  or wet  $\text{C}_3\text{H}_8$  as fuel. In addition, and as expected due to exsolution intrinsic advantages, the functionalized material showed a notable resistance against coke deposition. Other works have also demonstrated this core–shell (metal–metal oxide) exsolution. Namely, NiFe/ $\text{FeO}_x$  nanoparticles from  $\text{Pr}_{0.4}\text{Sr}_{1.6}(\text{NiFe})_{1.5}\text{Mo}_{0.5}\text{O}_{6-\delta}$  double perovskites for their use as  $\text{CO}_2$  electrolysis cathodes in SOECs<sup>89</sup> or even Co/ $\text{CoO}_x$  in an interesting work involving porous nanotubular webs of double perovskite materials ( $\text{PrBa}_{0.5}\text{Sr}_{0.5}\text{Co}_{0.2}\text{Fe}_{1.8}\text{O}_{5+\delta}$ ).<sup>90</sup>

In summary, although multi-elemental exsolution is in its initial stages of development, it brings a promising opportunity for a more rational and efficient design of nanocatalysts *via in-situ* exsolution. The intrinsic advantages of exsolution, together with the ability to control the morphological and/or compositional properties of the exsolved nanoparticles, either alloys or non-alloyed multi-elemental structures, pave the path for expanding the potential applications of this kind of





catalysts, leading to more efficient, highly active and resistant functionalized materials.

### 3. Exsolution of non-metallic nanoparticles

**a. Oxide exsolution.** In the previous section, the possibilities of tuning metallic nanoparticle composition by creating multi-elemental metallic nanocatalysts have been described. Alternatively, researchers have expanded the realm of exsolution to other non-metallic catalysts such as oxides, sulphides or phosphides. Although the literature on this specific topic remains limited to date, exsolution of these chemical compounds could greatly enhance the applicability of this method to a wider spectrum of catalytic applications. A good example has been oxide exsolution for the functionalization of positrodes in proton ceramic fuel cells.<sup>91</sup> These electrodes operate under wet air at temperatures around 500 °C,<sup>3,92</sup> conditions under which many metallic nanocatalysts are prone to reoxidation. Our group has been involved in the oxide exsolution of positrodes as part of the consortium of the M-Era.NET project FunKeyCat. One of the key aspects that we tried to unveil in this project was the control over cobalt oxide exsolution, which, compared with metallic cobalt exsolution, presents more

difficulties in terms of materials design. In metallic exsolution, simple thermodynamic calculations can easily predict which species can exsolve in a certain system.<sup>58</sup> For instance, in a perovskite with  $\text{La}_{0.6}\text{Sr}_{0.4}\text{Cr}_{0.8}\text{Co}_{0.2}\text{O}_{3-\delta}$  composition, treatment under an  $\text{H}_2$  atmosphere at 900 °C results only in the exsolution of metallic Co nanoparticles, based on thermodynamic predictions, corroborated with experimental evidence.<sup>58</sup> However, oxide exsolution in double perovskites leads to more complex formulations and can even result in multi-oxide exsolution. That was exemplified in one of the consortium works by Balcerzak *et al.* in which oxide exsolution was assessed in Lu-doped  $(\text{Ba},\text{La})\text{CoO}_3$ .<sup>35</sup>  $\text{Lu}^{3+}$  doping was used as a strategy to induce lattice strain based on an ionic radius mismatch. Fig. 4a and b show that these cobaltites present nanoparticles covering their surface in the as-synthesized form. The long annealing treatments (48 h, 1200 °C in static air) and the strain induced by Lu-doping already triggered the formation of oxide nanoparticles in the as-synthesized form.<sup>35</sup> Interestingly, when analyzing the nature of the exsolved nanoparticles with elemental mapping, several oxide compositions were found, clearly influenced by the presence of several perovskite phases in the pristine material.<sup>35</sup> Namely, Ba–Co–La–O rich

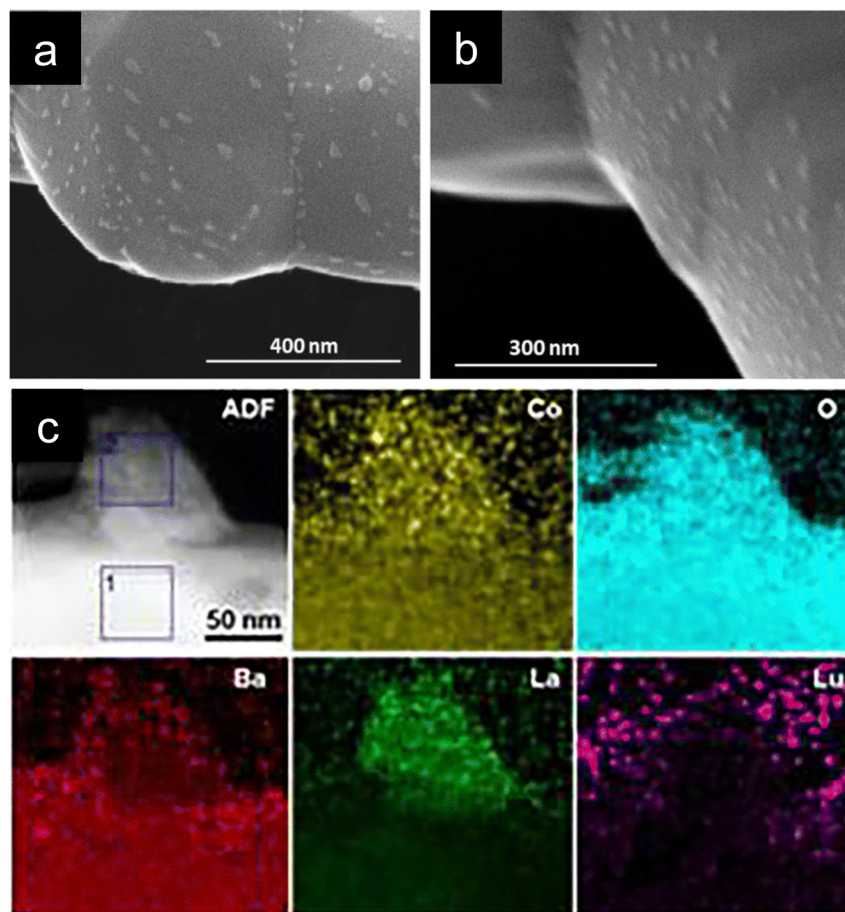


**Fig. 4** (a) and (b) SEM micrographs of  $\text{Ba}_{0.5}\text{La}_{0.4}\text{Lu}_{0.1}\text{CoO}_3$  depicting the oxide nanoparticle decoration over this double perovskite. (c) HAADF and EDX mappings of an exsolved nanoparticle composed of Co, La, Ba and O from  $\text{Ba}_{0.85}\text{La}_{0.15}\text{Co}_{0.75}\text{Lu}_{0.25}\text{O}_{3-\delta}$ . Reproduced from ref. 35 with permission from the Royal Society of Chemistry.



nanoparticles were exsolved from  $\text{Ba}_{0.85}\text{La}_{0.15}\text{Co}_{0.75}\text{Lu}_{0.25}\text{O}_{3-\delta}$  (Fig. 4c), whereas nanoparticles with low La content were exsolved from  $\text{Ba}_{0.4}\text{La}_{0.6}\text{Co}_{0.85}\text{Lu}_{0.15}\text{O}_{3-\delta}$ .<sup>35</sup> These results highlight the intricate nature of these systems, providing valuable insights that can guide future improvements and optimizations.

The thermodynamics of oxide exsolution were initially assessed by Tsvetkov *et al.*<sup>93</sup> for  $\text{Pr}_{1-x}\text{Ba}_{1-x}\text{Co}_2\text{O}_{6-\delta}$ , a much more well-known cobalt-based double perovskite.<sup>94–96</sup> In their work, Tsvetkov *et al.* achieved oxide exsolution after treating the  $\text{PrBaCo}_2\text{O}_{6-\delta}$  sample at 1000 °C in an atmosphere with  $p\text{O}_2 = 10^{-3}$  atm, whereas in their case, oxygen annealing did not lead to any exsolution. Based on thermodynamic calculations and oxygen content thermogravimetric data under different conditions, the authors identified these 30–40 nm nanoparticles as CoO, although depending on the temperature and  $p\text{O}_2$  used,  $\text{Co}_3\text{O}_4$  could also be formed.<sup>93</sup> However, recent works illustrate that this type of preliminary calculations might not be enough to predict the nature of the oxide-exsolved nanoparticles. In this sense, results found in the literature show that different compositions can be obtained from almost identical perovskite materials. For instance, Zhou *et al.* obtained  $\text{BaCoO}_{3-\delta}$  exsolved nanoparticles (identified through Raman spectroscopy) from  $\text{PrBa}_{0.8}\text{Ca}_{0.2}\text{Co}_2\text{O}_{5+\delta}$  used as positrodes in PCECs.<sup>97</sup> In a work by the same group, Hyuk Kim *et al.* also obtained exsolved  $\text{BaCoO}_{3-\delta}$ , which greatly promoted the electrocatalytic activity of these positrodes, through a water-induced surface modification.<sup>91</sup> The treatment involved exposure to 3 vol%  $\text{H}_2\text{O}/\text{air}$  for 3 h at 600 °C, resulting in particles smaller than 100 nm, which remained stable after operation at a constant cell voltage (0.65 V) for 230 h.<sup>91</sup> Despite the promise, it remains unclear why Tsvetkov's predictions pointed to  $\text{Co}_3\text{O}_4/\text{CoO}$  exsolution from  $\text{Pr}_{1-x}\text{Ba}_{1-x}\text{Co}_2\text{O}_{6-\delta}$ , whereas Liu's group obtained  $\text{BaCoO}_3$  exsolutions from  $\text{PrBa}_{0.8}\text{Ca}_{0.2}\text{Co}_2\text{O}_{5+\delta}$ . The same group also obtained  $\text{BaCoO}_3$  exsolution from  $\text{Pr}_{1-x}\text{Ba}_x\text{CoO}_{3-\delta}$  thin-film coatings used for enhancing the electrocatalytic activity of  $(\text{La}_{0.6}\text{Sr}_{0.4})_{0.95}\text{Co}_{0.2}\text{Fe}_{0.8}\text{O}_{3-\delta}$ .<sup>98</sup> Thus, Ca-substitution at the A-site could be ruled out as a possible reason for forming  $\text{BaCoO}_3$  instead of binary cobalt oxides. More recently, water-mediated exsolution has also been employed to functionalize alkali-metal doped BCFZY  $\text{A}_x\text{Ba}_{1-x}\text{Co}_{0.4}\text{Fe}_{0.4}\text{Zr}_{0.2-y}\text{Y}_y\text{O}_{3-\delta}$  (A = Li, Na, and K) with  $\text{BaO}_x$  nanoparticles.<sup>99</sup> Here, the choice of dopant highly affected the morphology of the exsolved nanoparticles. Li-doped and K-doped resulted in nanoparticles of 166 and 84 nm, respectively, whereas Na-doped size was too small for proper image analysis. This water-mediated exsolution (under 3%  $\text{H}_2\text{O}$  wet air, 600 °C) resulted in faceted nanoparticles. The authors ascribed the formation of  $\text{BaO}_x$  exsolved nanoparticles to the creation of oxygen and barium vacancies resulting from the acceptor doping strategy on the A-site. Based on DFT calculations, the authors demonstrated that Li and K doping decreased the energetics of barium and oxygen vacancy formation, thus increasing the driving force for  $\text{BaO}_x$  exsolution. In particular, the K-doped sample showed a remarkable decrease in polarization resistance (44%) after 5 h of treatment in wet conditions, revealing the positive impact of  $\text{BaO}_x$  exsolution on the electrochemical performance of PCFC.<sup>99</sup>

Based on these results, it is clear that more systematic experimental studies and computational calculations on oxide exsolution from perovskites are needed to discern the effects of the different processing conditions ( $p\text{O}_2$ , moisture, temperature) and material-related aspects (strain, A-site deficiency) on oxide exsolution. It will be critical to obtain processing guidelines to aid a targeted exsolution of a specific compound.

Oxide exsolution has also been achieved from non-perovskite materials. Namely,  $\text{PrO}_x$  was exsolved from  $(\text{Ce}_{0.9}\text{Gd}_{0.1})_{1-x}\text{Pr}_x\text{O}_{2-\delta}$ , significantly reducing the polarization resistance of these electrodes used in solid-oxide electrochemical cells.<sup>100</sup>  $\text{PrO}_x$ -exsolved nanoparticles were obtained after thermal treatments of 800 °C for 50 h in air. The particles are transformed into elongated needle-like nanoparticles by increasing the treatment time to 200 h.<sup>100</sup>

**b. Sulphide exsolution.** The formation of sulphide nanocatalysts has also been achieved *via* exsolution routes. The first report was by Sun *et al.*,<sup>101</sup> who obtained  $\text{WS}_2$  nanoparticles of around 5 nm size from  $\text{SrTiO}_3$ . The fabrication strategy followed several steps. First, W-doped  $\text{SrTiO}_3$  was treated with a 5%  $\text{H}_2\text{-N}_2$  flow at 800 °C for 10 h to induce the exsolution of W. Afterward, this sample was *in-situ* treated in  $\text{CS}_2$  flow at 350 °C for 2 h, using Ar as a gas carrier. This route proved to be effective, generating 61 particles/1000  $\text{nm}^2$ .<sup>101</sup> Exsolution combined with sulphidation could be a promising route for increasing the robustness of transition metal dichalcogenides, which are excellent catalysts in many relevant processes such as hydrogen evolution reaction.<sup>102</sup> More recently, CdS nanodots have been fabricated *via* exsolution at room temperature.<sup>36</sup> Here, the authors used  $\text{La}_{0.4}\text{Sr}_{0.4}\text{Cd}_{0.05}\text{Ti}_{0.95}\text{O}_{3-\delta}$ , exhibiting a cotton-ball-like morphology as the parent perovskite for the exsolution process and  $\text{Na}_2\text{S}$  as a sulphur precursor, which was contained in a vessel along with a vial containing the perovskite. Upon the addition of HCl,  $\text{H}_2\text{S}$  was formed, and after 5 min the perovskite changed color from white to yellow as an initial indication of CdS formation of around 3.5 nm nanoparticle size.<sup>36</sup> Different from the previous work, sulphide nanoparticle formation was achieved in a single exsolution step, without the need for initial reduction in a hydrogen stream, and importantly, at room temperature.<sup>36</sup> CdS exsolved  $\text{La}_{0.4}\text{Sr}_{0.4}\text{Cd}_{0.05}\text{Ti}_{0.95}\text{O}_{3-\delta}$  materials showed great promise as photocatalysts for  $\text{H}_2$  production.<sup>36</sup>

**c. Phosphide exsolution.** A similar strategy as applied by Sun *et al.*<sup>101</sup> to obtain  $\text{WS}_2$  nanoparticles was followed by Zhang *et al.* to obtain CoP using a combined exsolution-phosphidation protocol.<sup>103</sup> The exsolution was performed on  $(\text{PrBa}_{0.5}\text{Sr}_{0.5})_{0.95}\text{-}(\text{Co}_{1.5}\text{Fe}_{0.5})_{0.95}\text{Co}_{0.05}\text{O}_{5+\delta}$  nanofibers at 350 °C for 2 h under 5%  $\text{H}_2$  flow. Afterwards, the phosphidation process was conducted using  $\text{NaH}_2\text{PO}_2\text{-H}_2\text{O}$  as the phosphorus precursor in a tube furnace at 300 °C under an Ar flow for 2 h. This catalyst exhibited high catalytic activity in several electrochemical reactions carried out in alkaline media, showing high stability for water splitting reaction during 12 h.<sup>103</sup>

These works have served as a proof of concept for the exsolution of new chemistries (oxides, sulphides, and phosphides), which could greatly expand the benefits of these



methods to other catalytic processes. However, conducting more systematic analyses, where the treatments are evaluated under different conditions, will be crucial for a better understanding of this process, unveiling the mechanisms behind the direct exsolution of these non-metallic compounds.

#### 4. Non-thermally driven nanoparticle exsolution

Metallic nanoparticle exsolution has been conventionally triggered by thermal reduction treatments in a (diluted)  $H_2$  atmosphere. Different times, temperatures and  $H_2$  partial pressures have been utilized, which, depending on the perovskite system, have resulted in varying particle sizes, nanoparticle dispersion or even particle morphology (see Section 1). Probably the most studied perovskite system in exsolution has been  $La_{1-y}A_yTi_{1-x}Ni_xO_{3-\delta}$  in which  $A = Sr, Ca$  or  $Ce$ , often with A-site deficiency to favor the formation of exsolved nanoparticles. Anyhow, this perovskite class requires high temperatures and long treatments to reach nanoparticle exsolution. For instance,  $La_{0.43}Ca_{0.37}Ni_{0.06}Ti_{0.94}O_{3-\gamma}$  electrodes required reduction with hydrogen at  $900\text{ }^\circ\text{C}$  for 20 h to reach a population of around 100 particles per  $\mu\text{m}^2$ .<sup>37</sup> These dispersion values are low

compared to other perovskite systems in which at similar temperature conditions and shorter exposure times show a 6-fold improvement.<sup>31</sup> In this sense, several studies have attempted to reach higher nanoparticle populations by using unconventional approaches in which exsolution is triggered by other phenomena different from thermal reduction. These are electrochemical-driven, plasma and microwave-assisted exsolution (Fig. 5a) and laser-induced exsolution. Most of these treatments allow for exsolution in the absence of an  $H_2$  atmosphere and at milder temperatures, reaching remarkable nanoparticle dispersions.

**a. Electrochemical poling.** The first report in which nanoparticle exsolution was probably achieved *via* a non-conventional route was the work by Myung *et al.*, in which exsolved nanoparticles were obtained by electrochemical switching.<sup>37</sup> For that purpose, the authors built a solid-oxide electrochemical cell, in which the fuel electrode was  $La_{0.43}Ca_{0.37}Ni_{0.06}Ti_{0.94}O_{3-\gamma}$  from which Ni exsolution was assessed. By applying 2 V under a 50%  $H_2O/N_2$  atmosphere at  $900\text{ }^\circ\text{C}$  for 150 s, the authors achieved exsolution of Ni particles with a higher nanoparticle dispersion compared to conventional heating (*ca.* 350 *vs.* 100 particles per  $\mu\text{m}^2$ ,

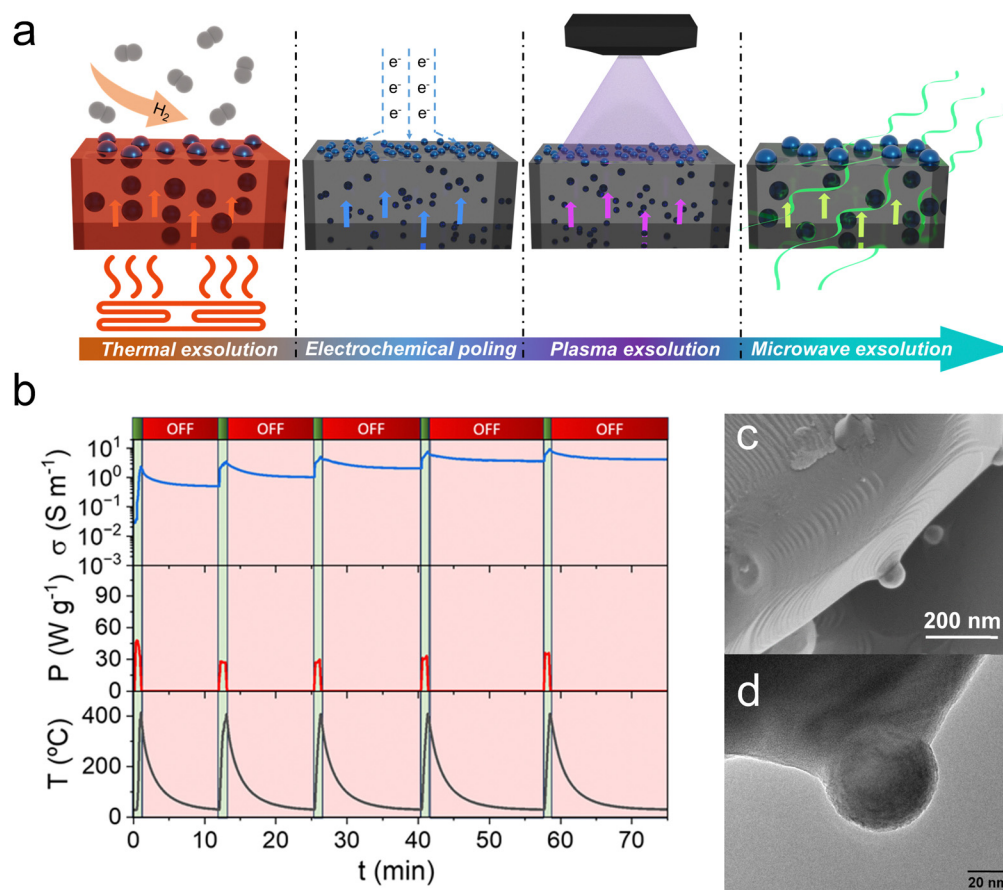


**Fig. 5** (a) Schematic of the different approaches used to drive the exsolution of metallic nanoparticles. (b) Plot of five microwave pulses utilized to drive the exsolution of Ni nanoparticles from  $La_{0.43}Ca_{0.37}Ni_{0.06}Ti_{0.94}O_{3-\delta}$ . The microwave-cavity reactor in which these experiments were performed allowed measuring the materials electrical conductivity during the microwave-driven exsolution process. This process was performed at low temperatures ( $400\text{ }^\circ\text{C}$ ) and just in the presence of inert  $N_2$  flow, avoiding the use of  $H_2$ . (c) SEM and (d) TEM micrographs depicting spherical Ni nanoparticles exsolved by applying microwave radiation. Adapted from ref. 40.



respectively).<sup>37</sup> The high dispersion in such short exposure times evidenced the benefits of this novel exsolution approach in the absence of H<sub>2</sub>. This work served as an illustrating example of a breakthrough in the field, opening new scientific questions. Since then, several research works have focused on understanding the interplay between electrochemical switching and metallic exsolution.<sup>104</sup> For instance, Summerer *et al.* studied Fe exsolution *via* electrochemical switching in La<sub>0.6</sub>Sr<sub>0.4</sub>FeO<sub>3-δ</sub> thin film electrodes.<sup>105</sup> The authors investigated the effects of cathodic bias using wet H<sub>2</sub> atmospheres, identifying several regimes depending on the applied bias. High cathodic polarization, low pO<sub>2</sub> and long exposure times helped promote metallic iron exsolution.<sup>105</sup> These electrochemical-driven exsolved particles could experience reversible oxidation/reduction by changes in the applied potential and gas atmosphere. Interestingly, the changes between the active and inactive iron states followed a hysteresis-like curve.<sup>105</sup>

Lu and co-authors have studied the effects of the applied potential on the exsolved nanoparticle dispersion in more detail using La<sub>0.43</sub>Ca<sub>0.37</sub>Ti<sub>0.94</sub>Ni<sub>0.06</sub>O<sub>3-δ</sub> electrodes.<sup>106</sup> The uniqueness of this work is that the authors designed an electrochemical device in such a way that the applied voltage was spatially graded. At 0 V (900 °C, 5 min exsolution), which correlates with pO<sub>2</sub> < 10<sup>-20</sup> atm (5% H<sub>2</sub> atmosphere), the exsolved nanoparticle population was equal to 90 particles per μm<sup>2</sup>. However, in the region where a higher cathodic potential of -1.37 V was applied (equivalent to a pO<sub>2</sub> of ca. 10<sup>-45</sup> atm), the nanoparticle population increased to 205 particles per μm<sup>2</sup>.<sup>106</sup> Interestingly, nanoparticle size did not suffer alterations when varying the voltage, indicating that on increasing the cathodic voltage, nucleation of the exsolved nanoparticles is promoted but not the growth of the exsolved nanoparticles. This fast nucleation driven by electrochemical switching was also confirmed in La<sub>0.52</sub>Ca<sub>0.28</sub>Ni<sub>0.06</sub>Ti<sub>0.94</sub>O<sub>3</sub> fibers compared to conventional exsolution, which helped increase the activity of these electrodes.<sup>107</sup> As commented above, in the work of Lu *et al.*, the particle size of exsolved Ni in La<sub>0.43</sub>-Ca<sub>0.37</sub>Ti<sub>0.94</sub>Ni<sub>0.06</sub>O<sub>3-δ</sub> electrodes was not affected by the applied potential.<sup>106</sup> However, this effect might be material-specific and/or heavily influenced by the gas atmosphere conditions. In a recent work by Kim *et al.*, electrochemical-driven exsolution was performed in La<sub>0.7</sub>Sr<sub>0.2</sub>Co<sub>0.2</sub>Fe<sub>0.8</sub>O<sub>3</sub> electrodes for SOECs.<sup>108</sup> Here, the authors report Co exsolution under cathodic bias. Quite interestingly, CoFe alloys were not formed. Moreover, the authors observed that increasing the applied voltage induces the growth of the exsolved nanoparticles.<sup>108</sup> At low cell voltages, -0.5 V for 10 min, exsolved nanoparticles of around 30 nm appeared on the surface of La<sub>0.7</sub>Sr<sub>0.2</sub>Co<sub>0.2</sub>Fe<sub>0.8</sub>O<sub>3</sub>.<sup>108</sup> The authors suggest that at such low voltages and before the point at which the electrochemical switching happens (-0.98 V) these Co nanoparticles are partially oxidized by H<sub>2</sub>O and/or CO<sub>2</sub> used for electrolysis. After this point, completely reduced Co nanoparticles are obtained, however, with a remarkable increase in nanoparticle size up to 200 nm observed at -1.5 V.<sup>108</sup>

In summary, electrochemical-driven exsolution is a promising tool for (but limited to) the functionalization of electrodes

in SOFCs, electrolyzers or other electrochemical devices. It has been proven under different atmospheres and applied cathodic voltages, and even using anodic shocks.<sup>109</sup> The reported scientific evidence clearly indicates that electrochemical switching accelerates exsolved nanoparticle exsolution, obtaining remarkable dispersion in a few minutes. However, more fundamental works are required to decipher the underlying mechanisms of electrochemical plating, unveiling the role of process conditions and material properties on the exsolution extent.

**b. Plasma-assisted exsolution.** Plasma-driven exsolution was first reported by Kyriakou *et al.*, using La<sub>0.43</sub>Ca<sub>0.37</sub>Ni<sub>0.06</sub>Ti<sub>0.94</sub>O<sub>3-δ</sub> as a perovskite model material.<sup>39</sup> Ni exsolution was first performed by applying plasma in a N<sub>2</sub> atmosphere at 650 °C for 1 h and compared to conventional exsolution in a H<sub>2</sub> atmosphere for 2 h. Under these conditions, the plasma-assisted process led to the formation of exsolved Ni nanoparticles of ca. 20 nm, with a dispersion of 160 particles per μm<sup>2</sup>, whereas using the conventional treatment exsolution, 80 particles per μm<sup>2</sup> of around 11 nm were exsolved. These results showed that plasma treatments accelerate exsolution, with higher dispersion values and larger nanoparticles in shorter times.<sup>39</sup> The authors also evaluated different plasma sources, namely, using powers of 50, 125 and 200 W in N<sub>2</sub> gas flow and 30 W powered Ar plasma (always for 60 min at 650 °C). Interestingly, the Ar plasma, with lower power input, resulted in a higher nanoparticle dispersion (ca. 900 particles per μm<sup>2</sup>) and particle sizes around 8 nm. According to the authors, this higher driven force of Ar plasma is caused by a higher (~100 times larger) electron and ion density if compared to N<sub>2</sub> plasma. This, in turn, triggers a 100 times higher electron and cation flux to the surface, thus enhancing nanoparticle exsolution.<sup>39</sup> In brief, this exsolution mechanism by plasma creates an accumulation of electrons at the surface of the perovskite. This generates a negatively charged layer on the surface, which induces metallic nucleation.<sup>39</sup>

A second work that deals with plasma-driven Ni exsolution is by Khalid *et al.* using an identical composition La<sub>0.43</sub>Ca<sub>0.37</sub>Ti<sub>0.94</sub>Ni<sub>0.06</sub>O<sub>2.955</sub>.<sup>110</sup> Here, the exsolution was performed in Ar plasma (0.3 mbar vacuum pressure), applying a power of 40 W for times ranging from 10–20 min, and importantly, at room temperature. Even with just a 10 min treatment, it was possible to exsolve nanoparticles of ca. 20 nm and 60 particles per μm<sup>2</sup> dispersion, which increased to 510 particles per μm<sup>2</sup> by increasing the exposure time to 20 min.<sup>110</sup> This remarkable result achieved in such a short exsolution time and at such low temperatures illustrated the potential of plasma-assisted exsolution. In both works, the plasma-treated samples presented stable catalytic activity for CO<sub>2</sub> hydrogenation<sup>39</sup> and CO oxidation reactions.<sup>110</sup>

**c. Microwave-assisted exsolution.** Recently, a novel approach for nanoparticle exsolution based on using microwaves as reducing agents was developed.<sup>40</sup> The rationale was built upon our previous works in which microwave radiation was utilized to drive the reduction of trivalent-doped cerium oxides for hydrogen production based on redox thermochemical cycles.<sup>44</sup> Thus, this technique allows for the generation of oxygen vacancies in oxides, which is a key step in metallic



nanoparticle exsolution.<sup>53</sup> In these works, a microwave-cavity fixed bed reactor was utilized, in which metal-oxide reduction is performed with microwave radiation. A remarkable feature of this device is that it allows monitoring the electrical conductivity changes experienced by the oxide during exsolution without using any electrical contacts.<sup>40</sup> In this work, the exsolution was performed by applying short microwave pulses, applying between 30 and 50 W g<sup>-1</sup> of power per reduction cycle (Fig. 5b). These microwave pulses lasted less than 1 min, a period during which the temperature was rapidly raised to 400 °C. After the microwave supply was switched off, a new cycle was performed after the temperature reached RT. Fig. 5b shows 5 microwave cycles used for the exsolution experiments, with the power input, temperature reached and sample conductivity.<sup>40</sup> Surprisingly, even after the first pulse, Ni nanoparticle exsolution was inferred by XRD and SEM. In other words, exsolution was performed in less than one minute, aided by rapid microwave irradiation. This first microwave pulse resulted in nanoparticle populations of about 30 particles per μm<sup>2</sup> and sizes around 21 nm. These dispersion values are obviously far from ideal, especially if compared with the other methods described in previous sections. However, it should be kept in mind that the exposure times were less than one minute. Interestingly, by applying more pulses (up to five), the dispersion slightly decreased (25 particles per μm<sup>2</sup>) while the nanoparticle size slightly increased (ca. 33 nm), indicating that more pulses favoured nanoparticle growth rather than nucleation, Fig. 5c and d.<sup>40</sup> The catalytic activity of the microwave-treated samples also remained very stable over time when tested for the reverse water shift reaction.<sup>40</sup> This first work on microwave exsolution highlights the benefits of this technology, especially its requirement for short exposure times. In addition, hydrogen is not required, the system can work at ambient pressure and it is easily scalable, which are exciting benefits compared to other exsolution routes (Fig. 5a).

**d. Photo-induced exsolution.** Photo-induced Ag exsolution was reported on AgNbO<sub>3</sub> perovskites by Lu *et al.*<sup>38</sup> using the light emitted by the Xe lamp and 30 min time of irradiation (according to the authors, this treatment resulted in a temperature of 71 °C on the perovskite surface). After just 10 min of exposure time, the authors obtained an exsolution dispersion of about 125 particles per μm<sup>2</sup> of nanoparticles of around 10 nm.<sup>38</sup>

More recently, a similar approach was applied to a non-perovskite oxide (in section 6 this topic is covered in more detail). In this case, photo-thermal exsolution was utilized to exsolve precious metals, *viz.* Pt, Rh, and Ir, from WO<sub>3</sub>.<sup>111</sup> By applying an intense pulsed light-derived momentary photo-thermal treatment (reaching temperatures higher than 1000 °C), the exsolution process was achieved in an unprecedented short period of time of less than 20 ms.<sup>111</sup> This method resulted in exsolved nanoparticles of around 5 nm, which presented remarkable sensing performance in the detection of H<sub>2</sub>S.<sup>111</sup>

**e. Laser-induced exsolution.** Laser-induced exsolution was demonstrated on (La<sub>0.7</sub>Sr<sub>0.3</sub>)<sub>0.93</sub>Ti<sub>0.93</sub>Co<sub>0.07</sub>O<sub>3</sub> to obtain metallic Co nanocatalysts.<sup>112</sup> This method applied a two-laser (200 W power) treatment to exsolve nanoparticles in a fast manner,

achieving nanoparticle dispersions of about 75 particles per μm<sup>2</sup> after just 36 s of treatment. The perovskite with laser-induced Co exsolution exhibited stable electrocatalytic activity for the oxygen evolution reaction (OER), highlighting the potential benefits of this treatment in the functionalization of perovskite oxide electrocatalysts.<sup>112</sup>

**f. Ion irradiation alloy exsolution.** One of the latest breakthroughs in the field of exsolution has been the work by Wang *et al.* on the fabrication of exsolved alloy nanoparticles using ion irradiation.<sup>113</sup> The groundbreaking aspect of this novel exsolution technique was to create multi-elemental exsolved nanoparticles in which one of the metal constituents was introduced *via* an ion beam, rather than being obtained *via* conventional cation migration from the perovskite crystal structure.<sup>113</sup> In particular, the authors could exsolve *ca.* 2 nm FeNi<sub>x</sub> nanoparticles by applying a 10 keV Ni irradiation on a SrTi<sub>0.65</sub>Fe<sub>0.35</sub>O<sub>3</sub> thin film. Interestingly, by supplying 150 keV, the nanoparticles (*ca.* 3 nm) only consisted of metallic Fe, with all the Ni remaining in the SrTiO<sub>3</sub> substrate. This process was achieved by applying 10 keV Ni<sup>-</sup> and 150 keV Ni<sup>+</sup> beams on thin films at 800 °C for 1 h under high vacuum. The results indicate that careful control of the ion beam power is crucial for obtaining multi-elemental exsolved nanoparticles. In both cases, bulk exsolution (see Section 5) was observed, whose composition was also modulated by the ion beam power, namely, FeNi<sub>x</sub> with 10 keV and Fe nanoparticles with 150 keV. This indicates that this technology could be extremely helpful in tailoring the composition of endogenous exsolved nanoparticles, as well as serving as a tool to create multi-elemental exsolved nanoparticles *à la carte*. This could facilitate the fabrication of exsolved metallic alloys with tailored composition, which is a tedious task using conventional exsolution treatments (see Section 2) since B-site metal cations have different migration energies and cationic diffusions, which usually results in nanoparticles that are enriched by the cation with more favorable thermodynamics and kinetics for exsolution (*e.g.*, Ni over Fe).

## 5. Exsolution in solid–solid interfaces, endogenous nanoparticles and embedded metallic clusters

Nanoparticle exsolution has gained attention mostly due to its robustness, which provides high stability in high-temperature thermo- or electrochemical catalytic processes. Thus, it has been mainly employed to enhance the catalytic activity in gas–solid interfaces. However, recent works have shown that exsolved nanoparticles can also be employed to functionalize materials when completely embedded in solid–solid interfaces. There are two main paths to fabricate exsolved nanoparticles uniquely surrounded by one or more solid phases. First, by intrinsically generating the nanoparticles during the exsolution process that do not reach the surface generating sub-surface metallic nanoclusters or endogenous nanoparticles in the oxide bulk. The second approach involves the decoration of a surface *via* a conventional exsolution process followed by deposition of an oxide (or any other solid compound) over the functionalized surface, see Fig. 6a. While the former case was already reported a decade ago,<sup>114,115</sup> for the second approach, there is a unique



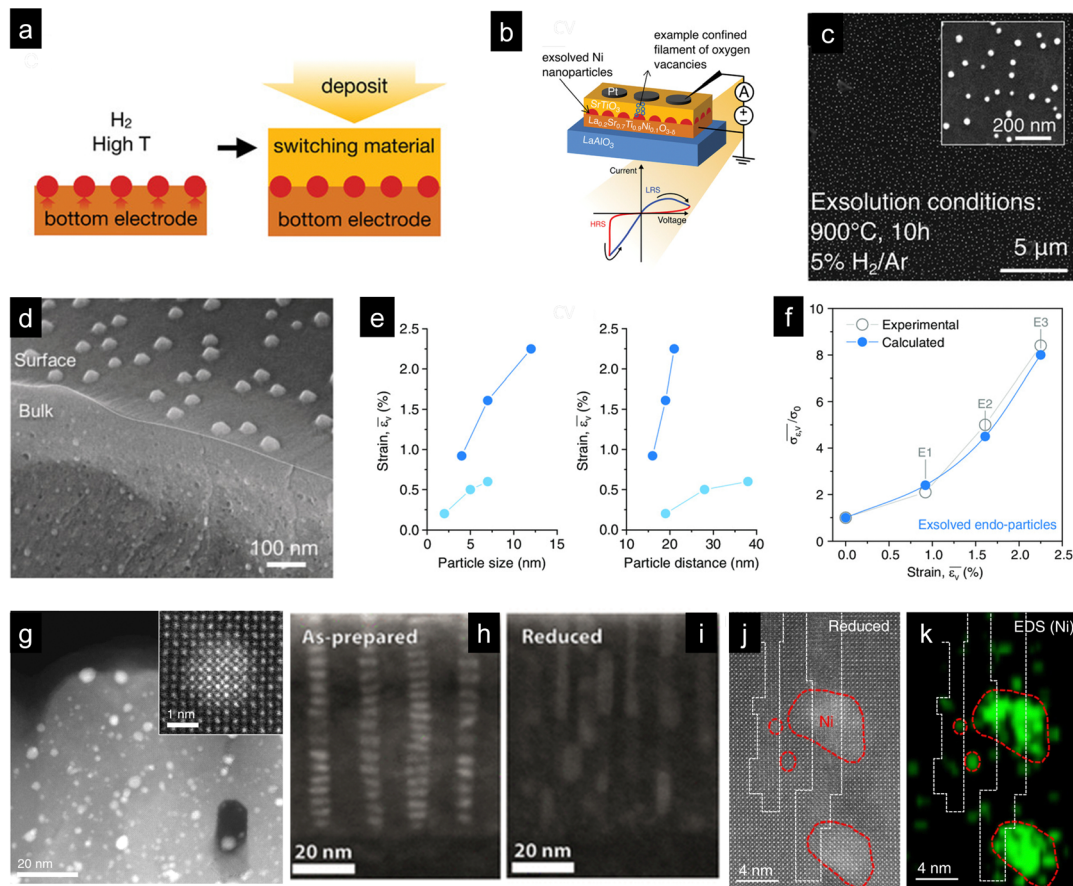


**Fig. 6** (a) Schematic depicting the fabrication strategy to functionalize the perovskite-based bottom electrode in resistive switches (b) with exsolved metallic nanoparticles. In the first step, the perovskite thin film,  $La_{0.2}Sr_{0.7}Ti_{0.9}Ni_{0.1}O_{3-\delta}$ , fabricated through pulsed laser deposition (PLD) on a  $LaAlO_3$  substrate was reduced to generate exsolved Ni nanoparticles. Afterwards, a second PLD thin film was deposited on top of the exsolved perovskite, rendering a solid–solid interface in which exsolved Ni nanoparticles were embedded. (c) SEM micrograph of Ni nanoparticle exsolution from the bottom electrode thin-film  $La_{0.2}Sr_{0.7}Ti_{0.9}Ni_{0.1}O_{3-\delta}$  thin film after reduction for 10 h at 900 °C. Reprinted with permission from ref. 6. (d) SEM micrograph depicting bulk and surface exsolution of Ni nanoparticles in  $La_{0.8}Ce_{0.1}Ni_{0.4}Ti_{0.6}O_3$  perovskite powders used as oxygen carriers in chemical looping syngas production. (e) Influence of particle size and interparticle distance of endogenous nanoparticles on strain. Dark blue dots represent endogenous nanoparticles created *via* exsolution, whereas light blue dots represent nanoparticles created by assembling and sintering. (f) Influence of strain generated with the exsolved endo-particles on the conductivity. Reproduced from ref. 44. (g) STEM-HAADF micrograph of a thin film with Pt exsolved clusters formed in a Pt-doped  $CaTiO_3$  film after a reduction treatment. The inset shows a metallic Pt cluster totally embedded in the perovskite thin film. Reproduced with permission from ref. 115. STEM-HAADF micrographs of  $SrTi_{0.9}Nb_{0.05}Ni_{0.05}O_{3-\delta}$  thin films before (h) and after reduction (i). Reprinted (adapted) with permission from M. L. Weber, M. Wilhelm, L. Jin, U. Breuer, R. Dittmann, R. Waser, O. Guillon, C. Lenser and F. Gunkel, *ACS Nano*, 2021, **15**, 4546–4560. Copyright 2021 American Chemical Society. (j) STEM-HAADF and (k) EDXS mapping of Ni clusters formed in a  $La_{0.2}Sr_{0.7}Ni_{0.1}Ti_{0.9}O_{3-\delta}$  thin film in anti-phase boundaries. Reproduced with permission from ref. 116.

report developed by Spring *et al.* from Prof. Rupp's group.<sup>6</sup> This specific work aimed at functionalizing the bottom electrode/switching oxide interface of a resistive switching device (Fig. 6b) to favor filament confinement, eventually improving their performance. The strategy here was to perform Ni exsolution, Fig. 6c, from  $La_{0.2}Sr_{0.7}Ti_{0.9}Ni_{0.1}O_{3-\delta}$  at different times and temperatures, resulting in thin films (fabricated through pulsed laser deposition (PLD) on a  $LaAlO_3$  substrate) with exsolved nanoparticles of various sizes and dispersions. The next step was depositing, also through PLD, a layer of amorphous  $SrTiO_3$  and, on top, a Pt electrode *via* sputtering. This nano-fabrication route was effective in improving cycle-to-cycle variability, which is one of the issues that this type of devices encounter.

Besides this work, most of the reports on metallic nanoparticle exsolution in solid–solid interphases are related to nanoparticles formed during the exsolution process or sometimes by carefully adjusting the process conditions. Perhaps the most relevant work covering this latter aspect is by Kousi *et al.*, who were able to exsolve Ni nanoparticles both at the perovskite surface and at the bulk of  $La_{0.8}Ce_{0.1}Ni_{0.4}Ti_{0.6}O_3$  perovskite powders (Fig. 6c). Interestingly, as depicted in Fig. 6c, the particles in the bulk, named “endogenous”, are smaller than the particles at the surface, namely, 13 and 45 nm, respectively.<sup>43</sup> To obtain a material with such morphology, authors strategized a set of intrinsic and extrinsic parameters that effectively resulted in the targeted objective: a perovskite with relatively low cationic diffusion (to favor bulk *versus*



surface exsolution), a high content of exsolvable metal transition cations on the B-site, A-site deficiency, and high exsolution temperatures (1000 °C) and exposure times (10 h) to help the nucleation and growth in the bulk, since this latter process has higher energy requirements than surface exsolution.<sup>43</sup> However, the beauty of this work relies not only on the smart materials design using the aforementioned combination of material-related properties and treatment conditions but also on the effect caused by the endogenous nanoparticles. By forming the endogenous Ni NPs, the authors induced tensile strain in the perovskite oxide, leading to an increase in the oxygen exchange capacity of these oxides. This enhancement in lattice oxygen release improved the methane partial oxidation activity in the chemical looping syngas production reactions in which these materials were tested. This enabled working at unprecedented low temperatures in methane-assisted chemical looping (450 °C).<sup>42</sup> These works unlocked a new functionality of nanoparticle exsolution, in which the nanoparticles are utilized to induce tensile strain in the oxide, where more conventionally, exsolution is aimed at catalyzing surface reactions.<sup>42</sup> This could be considered a major breakthrough in the field since there are not many available technologies to induce tensile strain in bulk oxides. Only a few works by Ishihara's group, in which gold nanoparticles were embedded in perovskite electrodes in SOFCs, have been reported to date.<sup>117,118</sup> In a recent work, Dalton and Neagu have evaluated the strain effects of both the exsolution-driven pathway and the route proposed by Ishihara's group.<sup>44</sup> Their modelling results allowed identifying the amount of strain produced when varying the nanoparticle size and the nanoparticle distance for both approaches and the impact of strain on the ion conductivity.<sup>44</sup> Strain increased with both increasing nanoparticle size and the interparticle distance (Fig. 6e), and the strain determined for the exsolution approach helped in enhancing the conductivity exponentially (Fig. 6f).

These works have revealed the great potential of using exsolution of endogenous nanoparticles as a strain-engineering strategy in metal oxides, which could be easily scaled up. Most works on strain engineering in oxides have been devoted to thin films, in which strain is usually induced by a lattice mismatch between the deposited oxide and the oxide substrate used. Indeed, this approach has been utilized to demonstrate the effects of strain on nanoparticle exsolution in thin films. For instance, Han *et al.* proved that compressive strain helped in increasing the nanoparticle dispersion compared with tensile strain,<sup>41</sup> revealing the benefits of precise strain engineering in the development of exsolved nanocatalysts.

Thin films have served as a magnificent playground for fundamental studies that helped in unveiling the factors governing metallic nanoparticle exsolution.<sup>119</sup> Moreover, the first reports on “bulk” exsolution of metallic nanoclusters were first observed in Pt-doped CaTiO<sub>3</sub> thin films by Katz *et al.*,<sup>115</sup> Fig. 6g. This work pioneered in revealing that Pt clusters not only formed as exsolved nanoparticles on the perovskite surface but could also form metallic clusters fully embedded in the oxide sub-surface.<sup>115</sup> Interestingly, after treatment in oxidation conditions, not all of these Pt nanoclusters re-dissolve back in

the perovskite bulk, indicating a low extent of reversibility of these “bulk” exsolution processes.

In some perovskite systems, nanoclusters have been identified even under pristine conditions after thin-film deposition. This is observed in the case of NiO<sub>x</sub> clusters that were observed in SrTi<sub>0.9</sub>Nb<sub>0.05</sub>Ni<sub>0.05</sub>O<sub>3-δ</sub> thin films.<sup>120</sup> This phase separation, Fig. 6h and i, occurred even before the reduction treatment, in which these B-site dopants formed columns of nanoclusters spontaneously.<sup>120</sup> According to the authors, these columns of oxidized nickel served as preferential spots for the exsolution of metallic Ni.<sup>120</sup> These results revealed an alternative mechanism for metallic nanoparticle exsolution in stoichiometric thin films, in which these capsule-like nanoclusters served as nuclei for metallic nanoparticle exsolution.<sup>120</sup> More recently, Guo *et al.* proved that by varying the deposition conditions (vacuum pressure) it was possible to also obtain different nanostructures embedded in the LaFe<sub>0.7</sub>Co<sub>0.1</sub>Ni<sub>0.1</sub>Ru<sub>0.05</sub>Pd<sub>0.05</sub>O<sub>3-δ</sub> thin-films. Namely, with pressures of 0.15 mTorr in the PLD process, self-assembled nanorods were obtained, whereas at 0.015 mTorr, core-shell NPs were observed. The outer shell was formed by a Ni-Co oxide, whereas the core was composed of Pd.<sup>121</sup>

Following thin-film studies on titanate-based perovskites, works have also focused on A-site deficient perovskites, such as (La<sub>0.2</sub>Sr<sub>0.7</sub>Ni<sub>0.1</sub>Ti<sub>0.9</sub>O<sub>3-δ</sub>).<sup>116</sup> In this case, the amount of exsolved nanoparticles was one order of magnitude higher (795 *vs.* 51 NPs per μm<sup>2</sup>) when comparing the non-stoichiometric and stoichiometric perovskites.<sup>116</sup> The authors ascribed this higher nucleation extent to the formation of anti-phase boundaries in the perovskite, which facilitated the diffusion of Ni to the surface.<sup>116</sup> Fig. 6j and k depict the HAADF-STEM and EDXS mappings for Ni, in which the antiphase boundaries in the perovskite are marked by a dashed line.<sup>116</sup> Authors observed the formation of Ni clusters in these regions that served as paths for the migration of Ni toward the surface of the perovskite in which they nucleate as exsolved nanoparticles, exhibiting high dispersion.<sup>116</sup> These studies on thin films revealed the concomitant formation of metallic clusters or endogenous nanoparticles as well as exsolved nanocatalysts on the surface for both stoichiometric and non-stoichiometric perovskite thin films. Even though, for each case, a different mechanism seems to determine the exsolution kinetics, it is clear that crystal defects are crucial in accelerating the exsolution of metallic nanoparticles. Thus, defect engineering emerges as a major tool for improving the extent of metallic exsolution, which could be smartly used for generating endogenous exsolved nanoparticles. Despite the promise, scaling up the observations obtained in thin-film fundamental studies might not be straightforward for bulk oxide materials. However, the promising results regarding exsolved endogenous nanoparticle formation in bulk perovskite oxygen carriers and its superior oxygen exchange capacity, demonstrated for chemical looping syngas production, illustrate the potential of this novel approach.

## 6. Exsolution from non-perovskite oxides

Exsolution from non-perovskite oxide materials has fewer publications dedicated to it,<sup>1</sup> yet it is a promising field of research.



For instance, it is especially relevant in oxides commonly used as supports for metal nanoparticles in thermocatalytic processes, such as CO<sub>2</sub> hydrogenation or hydrocarbon reforming. The latter are endothermic reactions that occur at high temperatures, usually resulting in nanoparticle agglomeration. Therefore, improving materials functionalization is crucial for developing more efficient and resistant catalysts, where the exsolution method can emerge as a promising alternative.

#### a. Exsolution from fluorites and fluorite-like structures.

Among the non-perovskites oxides employed for exsolution purposes, fluorite structures (AO<sub>2</sub>), such as CeO<sub>2</sub>, have to be highlighted due to their physicochemical properties and applicability. They show high thermal stability and redox activity ascribed to their high oxygen ion mobility, which is why they are often used to increase the ionic conductivity in electrochemical cells. These materials, combined with the appropriate precious metal, can be adequate catalysts for some thermocatalytic processes like olefin hydrogenation.<sup>122</sup> They are also involved in other important processes, such as the oxidation of pollutant gases, such as NO or CO, to generate less harmful ones (NO<sub>2</sub> and CO<sub>2</sub>), as it is done in three-way catalysts in vehicles.<sup>123</sup>

In addition, these materials are widely employed in high-temperature electrocatalytic processes.<sup>122</sup> Conventionally, doping is a usual procedure to improve the electrochemical properties of these materials. For instance, doping ceria with trivalent cations

such as gadolinium increases its ionic conductivity.<sup>124,125</sup> These materials are employed in a wide range of high-temperature processes in which surface reactions are crucial. Thus, functionalization with robust exsolved nanoparticles would be highly convenient. However, the low solubility of transition metal cations in ceria and other fluorite structures can limit the compositional tunability of these materials.

One of the first reports of exsolution in fluorite-type oxides was probably on Ru exsolution from pyrochlores.<sup>126</sup> This exsolution process was performed on Sm<sub>2</sub>Ru<sub>x</sub>Ce<sub>2-x</sub>O<sub>7</sub> (with  $x = 0, 0.1, 0.2,$  and  $0.4$ ), where 10% H<sub>2</sub> was employed to exsolve metallic Ru nanoparticles, showing a mean size of about 1–2 nm (Fig. 7a). This exsolved material was tested for dry methane reforming reactions, showing higher catalytic activity and stability when compared to impregnated catalysts, highlighting the potential benefits of exsolution in high-temperature thermocatalytic processes for syngas production.

Our group also reported Ru exsolution from ruthenium-doped ceria (Ru<sub>0.01</sub>Ce<sub>0.99</sub>O<sub>2- $\delta$</sub> ), which is the first publication on exsolution in CeO<sub>2</sub>.<sup>49</sup> Ru nanoparticles (5 nm) were exsolved with a 5% H<sub>2</sub> flow in Ar at 900 °C for 2 hours (Fig. 7b and c). This new catalyst was tested in chemical looping reforming of CH<sub>4</sub> coupled with CO<sub>2</sub> splitting, exhibiting higher CO<sub>2</sub> conversion at the same temperature as the undoped material and stable syngas production during 20 cycles. Remarkably, the well-anchored Ru nanoparticles remained morphologically

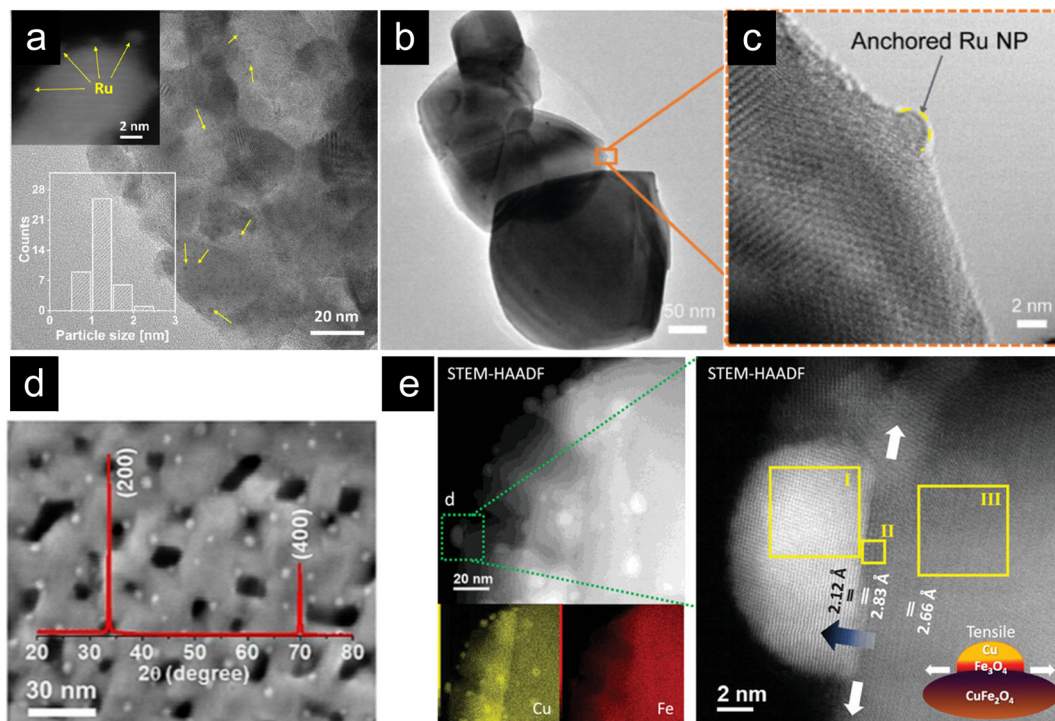


**Fig. 7** (a) TEM micrographs of Ru exsolution (10% H<sub>2</sub>, 700 °C, 1 h) from Sm<sub>2</sub>Ru<sub>0.2</sub>Ce<sub>1.8</sub>O<sub>7</sub>. Reprinted (adapted) with permission from M. A. Naeem, P. M. Abdala, A. Armutlulu, S. M. Kim, A. Fedorov and C. R. Müller, *ACS Catal.*, 2020, **10**, 1923–1937. Copyright 2020 American Chemical Society. (b) and (c) TEM micrographs of Ru exsolution (5% H<sub>2</sub>, 900 °C, 2 h) from Ru-doped CeO<sub>2</sub>. Reproduced from ref. 49 with permission from the Royal Society of Chemistry (d) SEM micrograph and XRD diffraction pattern of Ni nanoparticles exsolved from CeO<sub>2</sub> monoliths. Reproduced with permission from ref. 127. (e) STEM and EDXS map analysis of Cu exsolution from CuFe<sub>2</sub>O<sub>4</sub> spinels. Reproduced with permission from ref. 128.





unaltered (nanoparticle size of *ca.* 5 nm) after prolonged high-temperature treatment, evidencing that exsolution could be a promising superficial functionalization method for CeO<sub>2</sub>. Regarding Ru as the exsolvable cation, Hu *et al.*, tested a composite material consisting of mixed Sr<sub>2</sub>Fe<sub>1.5</sub>Mo<sub>0.5</sub>O<sub>6-δ</sub> with Gd<sub>0.1</sub>Ce<sub>0.9</sub>O<sub>2-δ</sub> to increase ionic conductivity, both doped with Ru.<sup>129</sup> They demonstrated that, under an H<sub>2</sub> or CH<sub>4</sub> atmosphere at 800 °C, Ru metallic nanoparticles exsolved over the surface of both materials, generating a carbon high-resistant anode with better performance compared to unaltered perovskites for methane conversion. This was the first work in which dual exsolution has been proven. On the other hand, changing the doping metal to Rh can generate efficient catalysts for hydrogen production through hydrocarbon steam reforming. Kim *et al.* used a rhodium-doped (8 wt%) ceria to generate exsolved nanoparticles (~3 nm) under a 10% H<sub>2</sub> atmosphere.<sup>130</sup>

As described in previous sections, Ni is the most common cation for exsolution in perovskites. Nevertheless, doping ceria or zirconia with transition metals such as Ni, Fe, or Co can be challenging due to the notable difference in ionic radius with host cations (Ce<sup>4+</sup> or Zr<sup>4+</sup> vs. Ni<sup>2+</sup>).<sup>131</sup> This size variation may limit the solubility and usually triggers the formation of secondary phases.<sup>132</sup> However, two works report Ni introduction in ceria oxides, using different conditions and showing some drawbacks. Qi *et al.*<sup>133</sup> reached 1000 °C to achieve metallic Ni exsolution under 5% H<sub>2</sub> in Ar flows, while Xiao *et al.*<sup>127</sup> tests involved the use of pure hydrogen. Although both reports represent a significant advance in Ni exsolution from fluorite-type oxides, the first approach<sup>133</sup> suffers from Ni agglomeration when a 0.2% (wt) doped catalyst is used for CO<sub>2</sub> direct electrolysis. The second approach<sup>127</sup> reports the partial oxidation of Ni when exposed to CH<sub>4</sub>, reducing the amount of active catalyst available. One exciting aspect of the work of Xiao *et al.* is that they fabricated porous single-crystalline Ni<sub>x</sub>Ce<sub>1-x</sub>O<sub>2</sub> monoliths with high porosity (*ca.* 68%), from which they exsolved 4 nm Ni nanoparticles (Fig. 7d).<sup>127</sup> This is relevant since obtaining highly porous single-phase oxides remains a challenge, especially when several cations are employed for the exsolution of multicomponent metallic nanoparticles. Finding a fabrication route that can yield exsolved materials with high specific surface areas will be a breakthrough in the field since it will expand the use of exsolution to other low-temperature processes in which the control over porosity is crucial.

Furthermore, NiO exsolution on CeO<sub>2</sub>-based structures was achieved thermally without reducing agents. In this case, Gd<sub>0.2-x</sub>Ni<sub>x</sub>Ce<sub>0.8</sub>O<sub>2-δ</sub> heated to 1250 °C exsolves Ni-rich nanoparticles, which, due to the high-temperature annealing under oxidizing conditions (air), resulted in NiO exsolution. Further reduction in hydrogen at 650 °C is needed (as in other common functionalization methods) to generate the final Ni nanoparticles (~15 nm). This could be a promising approach to lower the operation temperature in fuel cell performance (up to 500 °C).<sup>134</sup>

Finally, as discussed in Section 2, binary alloy exsolution has recently been achieved by Lee *et al.*<sup>135,136</sup> More specifically,

PtRu alloyed nanoparticles were obtained from Ce<sub>0.9</sub>Gd<sub>0.1</sub>O<sub>2-δ</sub> (CGO) for its use as a catalyst in the commercial diesel reforming process. Interestingly, after demonstrating the effective introduction of both Pt and Ru into the CGO lattice, exsolution of ~10 nm nanoparticles occur during the reaction, resulting in an *in-situ* exsolution. The generated PtRu alloy exhibited high conversions (even at low reaction temperatures) and excellent stability during long operation times (up to 200 h).

Regarding other fluorite structures, such as the previously stated ZrO<sub>2</sub>, exsolution of Ni metal has also been reported. It is common to find the ZrO<sub>2</sub> structure doped with Y<sup>3+</sup> (YSZ) as it imparts phase stability to the ceramic material at high temperatures.<sup>131</sup> Joo *et al.* demonstrated that YSZ can be doped up to 3% with Ni and, as in perovskites, an H<sub>2</sub> atmosphere would generate Ni metallic nanoparticles. These nanoparticles, between 20–50 nm size, were tested as catalysts for dry reforming of methane, exhibiting twofold higher activity than conventional Ni-YSZ cermets at 800 °C.<sup>131</sup>

**b. Exsolution from spinels.** Spinel (AB<sub>2</sub>O<sub>4</sub>) are also interesting oxide structures prone to exsolution due to some characteristics such as good oxidation resistance and structure stability while having reasonable electrical conductivity and high electrocatalytic activity when operated at high temperatures.<sup>128</sup> This work remarks the possibility of transition metal (*e.g.*, Cu and Fe) exsolution from a spinel matrix. Previously, Gan *et al.* demonstrated the exsolution of Fe nanoparticles at 800 °C from a FeVO<sub>4</sub> structure, which, in a reduction environment, got reduced to Fe/FeV<sub>2</sub>O<sub>4</sub> spinel.<sup>137</sup> This material is then used in steam electrolysis with better results than the widely used perovskite (La<sub>0.75</sub>Sr<sub>0.25</sub>)<sub>0.97</sub>Cr<sub>0.5</sub>Mn<sub>0.5</sub>O<sub>3-δ</sub>, in terms of conductivity and current density, although it does not outperform Ni-YSZ. It is, in addition, a redox reversible structure, from FeVO<sub>4</sub> (when oxidized), to Fe/FeV<sub>2</sub>O<sub>4</sub> (when reduced); therefore the catalysts can be potentially regenerated.<sup>137</sup> Finally, Cu exsolution from a spinel structure has been recently published (Fig. 7e).<sup>128</sup> CuFe<sub>2</sub>O<sub>4</sub> was treated under a 50% CO<sub>2</sub>/10% H<sub>2</sub>O atmosphere in an Ar flow for co-electrolysis, resulting in Cu/Fe<sub>3</sub>O<sub>4</sub> cermet exsolution. This material was found to have higher selectivity to CO than Fe<sub>3</sub>O<sub>4</sub>; however, its activity could not be compared to that of Cu oxide since it was not active under the applied test conditions.<sup>128</sup> The abovementioned reports on the exsolution of fluorites or spinels are good examples of how exsolution is not limited to perovskite oxides, and alternative metal oxides can be considered for their functionalization with *in-situ* exsolved nanoparticles.

## Outlook and future perspectives

Nanoparticle exsolution has gained considerable attention in the last decade as a catalyst fabrication route, assuring high structural robustness and long-term catalytic activity. It was initially explored mainly for high-temperature electrochemical conversion and storage devices, but rapidly, its applications expanded to other relevant thermocatalytic reactions, such as hydrocarbon reforming, CO<sub>2</sub> hydrogenation, chemical looping



syngas production or ammonia synthesis, just to name a few. Furthermore, it has been employed to functionalize other electrochemical devices, such as gas sensors or resistive switches, illustrating the broad applicability of this method. Regardless of the field of application, in this work, we have summarized the most promising research avenues in which efforts have been put in the last few years. We have identified six new trends, but other relevant aspects of nanoparticle exsolution are also currently under investigation. Our focus has been on identifying those technological modifications that we consider will have a high impact in the following years. Some of them are related to improving the exsolution extent by lowering the energy input required to generate nanoparticles or by making the process much faster under milder conditions. These non-thermal technologies show great promise for achieving high exsolution extents in very short exposure times. Despite the promise, more systematic and thorough experiments are required to better understand these new physico-chemical processes and their interaction with the exsolution mechanism. Regarding materials design, it is crucial to gain further understanding of the evolution of nanoparticles over time and the influence that intrinsic properties have on the stability of exsolution. As recently pointed out by Weber and co-authors, Ni exsolution from p-type and n-type perovskites have different coalescence dynamics,<sup>138</sup> which might in turn pose limitations on the long-term durability of the nanoparticles. Therefore, it is crucial to obtain materials design guidelines that ensure that NPs are properly anchored, avoiding isolated growth on specific spots, *e.g.*, grain boundaries that in turn will limit the catalytic activity of the exsolved nanoparticles. In this respect, high throughput synthesis could be a useful tool to accelerate materials discoveries and obtain the most efficient synthesis protocols, which might be material and application specific.

A second important aspect considered in this work is the expansion of nanoparticle exsolution to other chemistries. We have focused both on the support, non-perovskite oxides, and the nature of the exsolved nanoparticles, *i.e.*, non-metallic nanoparticles. This direction will have a high impact since many catalytic processes do not rely on metallic nanoparticles or perovskite supports. Furthermore, exsolution from non-oxide supports will be essential to advance in this direction. Their development, combined with computational tools<sup>139</sup> that accelerate materials discoveries and spectroscopic operando techniques to unveil the mechanism of nanoparticle exsolution from other non-oxide compounds, will be essential in this matter.

Finally, it is crucial to continue advancing metallic exsolution to unlock further functionalities. Fabrication of shape-controlled or multicomponent nanoparticles is a major aspect requiring more fundamental investigation to better understand and control these processes. The same applies to bulk exsolution, which has emerged as a remarkable tool for strain-engineering oxides on a large scale. This fact proves that exsolution can be successfully employed beyond surface modifications. In this respect, new synthetic routes that will allow for the fabrication

of complex oxides with high surface area while guaranteeing phase purity will be essential for further expanding the exsolution method to other processes. This will be especially relevant in mild temperature processes where fine-tuning the textural properties is paramount for achieving relevant catalytic activities. However, especially in the case of perovskite oxides, high temperatures (>1000 °C) are required to avoid phase segregation, which usually results in low specific surface areas (<5 m<sup>2</sup> g<sup>-1</sup>), limiting its applicability in many chemical reactions occurring at low temperatures.

These six research directions are expected to impact the fields of materials science, electrochemistry and catalysis in a wide range of applications. In several cases, many of them will be developed in combination, unlocking unprecedented material functionalities. These new research trends, at the forefront of materials design, combined with more conventional developments will help in expanding the knowledge and applicability of nanoparticle exsolution in the following years.

## Data availability

No primary research results, software or code have been included and no new data were generated or analysed as part of this review.

## Conflicts of interest

There are no conflicts of interest to declare.

## Acknowledgements

The project that gave rise to these results received the support of a fellowship from the “la Caixa” Foundation (ID 100010434). The fellowship code is LCF/BQ/PI20/11760015. Financial support by the Spanish Ministry of Science and Innovation (PID2022-139663OB-100 and CEX2021-001230-S grant funded by MCIN/AEI/10.13039/501100011033) and by Generalitat Valenciana (CIPROM/2022/10) is gratefully acknowledged. Blanca Delgado-Galicia acknowledges the funding provided by the SECAT Grants Program for the Completion of Master’s Thesis in Catalysis.

## References

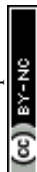
- 1 K. Kousi, C. Tang, I. S. Metcalfe and D. Neagu, *Small*, 2021, 2006479.
- 2 J. H. Kim, J. K. Kim, J. Liu, A. Curcio, J. Jang, I. Kim, F. Ciucci and W. Jung, *ACS Nano*, 2021, 15, 81–110.
- 3 E. Vøllestad, R. Strandbakke, M. Tarach, D. Catalán-Martínez, M.-L. Fontaine, D. Beeaff, D. R. Clark, J. M. Serra and T. Norby, *Nat. Mater.*, 2019, 18, 23–26.
- 4 C. Solís, V. B. Vert, M. Balaguer, S. Escolástico, S. Roitsch and J. M. Serra, *ChemSusChem*, 2012, 5, 2155–2158.
- 5 X. Li, L. Dai, Z. He, W. Meng, Y. Li and L. Wang, *Sens. Actuators, B*, 2019, 298, 126827.
- 6 J. Spring, E. Sediva, Z. D. Hood, J. C. Gonzalez-Rosillo, W. O’Leary, K. J. Kim, A. J. Carrillo and J. L. M. Rupp, *Small*, 2020, 16, 2003224.
- 7 T. W. Hansen, A. T. DeLaRiva, S. R. Challa and A. K. Dartye, *Acc. Chem. Res.*, 2013, 46, 1720–1730.



- 8 G. Prieto, J. Zečević, H. Friedrich, K. P. De Jong and P. E. De Jongh, *Nat. Mater.*, 2013, **12**, 34–39.
- 9 D. Neagu, J. T. S. Irvine, J. Wang, B. Yildiz, A. K. Opitz, J. Fleig, Y. Wang, J. Liu, L. Shen, F. Ciucci, B. A. Rosen, Y. Xiao, K. Xie, G. Yang, Z. Shao, Y. Zhang, J. Reinke, T. A. Schmauss, S. A. Barnett, R. Maring, V. Kyriakou, U. Mushtaq, M. N. Tsampas, Y. Kim, R. O'Hayre, A. J. Carrillo, T. Ruh, L. Lindenthal, F. Schrenk, C. Rameshan, E. I. Papaioannou, K. Kousi, I. S. Metcalfe, X. Xu and G. Liu, *J. Phys. Energy*, 2023, **5**, 031501.
- 10 D. Neagu, T. S. Oh, D. N. Miller, H. Menard, S. M. Bukhari, S. R. Gamble, R. J. Gorte, J. M. Vohs and J. T. Irvine, *Nat. Commun.*, 2015, **6**, 8120.
- 11 T. Ruh, D. Berkovec, F. Schrenk and C. Rameshan, *Chem. Commun.*, 2023, **59**, 3948–3956.
- 12 Y. Nishihata, J. Mizuki, T. Akao, H. Tanaka, M. Uenishi, M. Kimura, T. Okamoto and N. Hamada, *Nature*, 2002, **418**, 164–167.
- 13 Y. Nishihata, J. Mizuki, H. Tanaka, M. Uenishi and M. Kimura, *J. Phys. Chem. Solids*, 2005, **66**, 274–282.
- 14 H. Tanaka, M. Uenishi, M. Taniguchi, I. Tan, K. Narita, M. Kimura, K. Kaneko, Y. Nishihata and J. Mizuki, *Catal. Today*, 2006, **117**, 321–328.
- 15 H. Tanaka, I. Tan, M. Uenishi, M. Taniguchi, M. Kimura, Y. Nishihata and J. Mizuki, *J. Alloys Compd.*, 2006, **408–412**, 1071–1077.
- 16 H. Tanaka, M. Taniguchi, M. Uenishi, N. Kajita, I. Tan, Y. Nishihata, J. Mizuki, K. Narita, M. Kimura and K. Kaneko, *Angew. Chem.*, 2006, **118**, 6144–6148.
- 17 U. G. Singh, J. Li, J. W. Bennett, A. M. Rappe, R. Seshadri and S. L. Scott, *J. Catal.*, 2007, **249**, 349–358.
- 18 J. Li, U. G. Singh, J. W. Bennett, K. Page, J. C. Weaver, J. Zhang, T. Proffen, A. M. Rappe, S. Scott and R. Seshadri, *Chem. Mater.*, 2007, **19**, 1418–1426.
- 19 B. D. Madsen, W. Kobsiriphat, Y. Wang, L. D. Marks and S. A. Barnett, *J. Power Sources*, 2007, **166**, 64–67.
- 20 J. Li, U. G. Singh, T. D. Schladt, J. K. Stalick, S. L. Scott and R. Seshadri, *Chem. Mater.*, 2008, **20**, 6567–6576.
- 21 T. Z. Shoklapper, C. P. Jacobson, S. J. Visco and L. C. Dejonghe, *Fuel Cells*, 2008, **8**, 303–312.
- 22 S. Miyoshi and M. Martin, *Phys. Chem. Chem. Phys.*, 2009, **11**, 3063.
- 23 W. Kobsiriphat, B. D. Madsen, Y. Wang, L. D. Marks and S. A. Barnett, *Solid State Ionics*, 2009, **180**, 257–264.
- 24 X. Ouyang and S. L. Scott, *J. Catal.*, 2010, **273**, 83–91.
- 25 W. Kobsiriphat, B. D. Madsen, Y. Wang, M. Shah, L. D. Marks and S. A. Barnett, *J. Electrochem. Soc.*, 2010, **157**, B279.
- 26 T. Jardiell, M. T. Caldes, F. Moser, J. Hamon, G. Gauthier and O. Joubert, *Solid State Ionics*, 2010, **181**, 894–901.
- 27 X. Lou, Z. Liu, S. Wang, Y. Xiu, C. P. Wong and M. Liu, *J. Power Sources*, 2010, **195**, 419–424.
- 28 D. M. Bierschenk, E. Potter-Nelson, C. Hoel, Y. Liao, L. Marks, K. R. Poeppelmeier and S. A. Barnett, *J. Power Sources*, 2011, **196**, 3089–3094.
- 29 I. Hamada, A. Uozumi, Y. Morikawa, A. Yanase and H. Katayama-Yoshida, *J. Am. Chem. Soc.*, 2011, **133**, 18506–18509.
- 30 W. Zhou, Z. Shao, F. Liang, Z. G. Chen, Z. Zhu, W. Jin and N. Xu, *J. Mater. Chem.*, 2011, **21**, 15343–15351.
- 31 A. López-García, L. Almar, S. Escolástico, A. B. Hungria, A. J. Carrillo and J. M. Serra, *ACS Appl. Energy Mater.*, 2022, **5**, 13269–13283.
- 32 Y. Gao, D. Chen, M. Saccoccio, Z. Lu and F. Ciucci, *Nano Energy*, 2016, **27**, 499–508.
- 33 S. Otto, K. Kousi, D. Neagu, L. Bekris, J. Janek and I. S. Metcalfe, *ACS Appl. Energy Mater.*, 2019, **2**, 7288–7298.
- 34 W. O'Leary, L. Giordano and J. L. M. Rupp, *J. Mater. Chem. A*, 2023, **11**, 21429–21442.
- 35 D. Balcerzak, I. Szpunar, R. Strandbakke, S. W. Saeed, C. Baziotti, A. Mielewczyk-Gryn, P. Winiarz, A. J. Carrillo, M. Balaguer, J. M. Serra, M. Gazda and S. Wachowski, *CrystEngComm*, 2023, **25**, 4306–4316.
- 36 S. Chattopadhyay, A. B. Naden, W. S. J. Skinner, G. Kerherve, D. J. Payne and J. T. S. Irvine, *Adv. Energy Mater.*, 2023, **13**, 1–9.
- 37 J. Myung, D. Neagu, D. N. Miller and J. T. S. Irvine, *Nature*, 2016, **537**, 528–531.
- 38 Y. Lu, Q. Shen, Q. Yu, F. Zhang, G. Li and W. Zhang, *J. Phys. Chem. C*, 2016, **120**, 28712–28716.
- 39 V. Kyriakou, R. K. Sharma, D. Neagu, F. Peeters, O. De Luca, P. Rudolf, A. Pandiyan, W. Yu, S. W. Cha, S. Welzel, M. C. M. Sanden and M. N. Tsampas, *Small Methods*, 2021, **2100868**.
- 40 A. López-García, A. Domínguez-Saldaña, A. J. Carrillo, L. Navarrete, M. I. Valls, B. García-Baños, P. J. Plaza-Gonzalez, J. M. Catala-Civera and J. M. Serra, *ACS Nano*, 2023, **17**, 23955–23964.
- 41 H. Han, J. Park, S. Y. Nam, K. J. Kim, G. M. Choi, S. S. P. Parkin, H. M. Jang and J. T. S. Irvine, *Nat. Commun.*, 2019, **10**, 1471.
- 42 K. Kousi, D. Neagu, L. Bekris, E. Cali, G. Kerherve, E. I. Papaioannou, D. J. Payne and I. S. Metcalfe, *J. Mater. Chem. A*, 2020, **8**, 12406–12417.
- 43 K. Kousi, D. Neagu, L. Bekris, E. I. Papaioannou and I. S. Metcalfe, *Angew. Chem., Int. Ed.*, 2020, **59**, 2510–2519.
- 44 S. J. Dalton and D. Neagu, *Adv. Energy Sustainability Res.*, 2022, **3**, 2200054.
- 45 K. J. Kim, H. Han, T. Defferriere, D. Yoon, S. Na, S. J. Kim, A. M. Dayaghi, J. Son, T.-S. Oh, H. M. Jang and G. M. Choi, *J. Am. Chem. Soc.*, 2019, **141**, 7509–7517.
- 46 D. Neagu, G. Tsekouras, D. N. Miller, H. Menard and J. T. Irvine, *Nat. Chem.*, 2013, **5**, 916–923.
- 47 W. O'Leary, L. Giordano, J. Park, S. S. Nonnenmann, Y. Shao-Horn and J. L. M. Rupp, *J. Am. Chem. Soc.*, 2023, **145**, 13768–13779.
- 48 B. Delgado-Galicia, A. López-García, A. J. Carrillo and J. M. Serra, *Solid State Ionics*, 2024, **410**, 116532.
- 49 A. J. Carrillo, L. Navarrete, M. Laqdiem, M. Balaguer and J. M. Serra, *Mater. Adv.*, 2021, **2**, 2924–2934.
- 50 Y. H. Kim, Y. Kang, S. Jo, H. Jeong, D. Neagu and J. Ha Myung, *Chem. Eng. J.*, 2022, **441**, 136025.
- 51 D. Neagu, V. Kyriakou, I. Roiban, M. Aouine, C. Tang, A. Caravaca, K. Kousi, I. Schreur-Piet, I. S. Metcalfe, P. Vernoux, M. C. M. van de Sanden and M. N. Tsampas, *ACS Nano*, 2019, **13**, 12996–13005.
- 52 R. Thalinger, M. Gocyla, M. Heggen, B. Klötzer and S. Penner, *J. Phys. Chem. C*, 2015, **119**, 22050–22056.
- 53 J. Wang, J. Yang, A. K. Opitz, W. Bowman, R. Bliem, G. Dimitrakopoulos, A. Nanning, I. Waluyo, A. Hunt, J. J. Gallet and B. Yildiz, *Chem. Mater.*, 2021, **33**, 5021–5034.
- 54 V. B. Vert, F. V. Melo, L. Navarrete and J. M. Serra, *Appl. Catal., B*, 2012, **115–116**, 346–356.
- 55 D. Neagu, E. I. Papaioannou, W. K. W. W. Ramli, D. N. Miller, B. J. Murdoch, H. Ménard, A. Umar, A. J. Barlow, P. J. Cumpson, J. T. S. S. Irvine and I. S. Metcalfe, *Nat. Commun.*, 2017, **8**, 1855.
- 56 R. Sažinas, K. B. Andersen and K. K. Hansen, *J. Solid State Electrochem.*, 2020, **24**, 609–621.
- 57 Y. Zhu, W. Zhou, R. Ran, Y. Chen, Z. Shao and M. Liu, *Nano Lett.*, 2016, **16**, 512–518.
- 58 A. J. Carrillo, K. J. Kim, Z. D. Hood, A. H. Bork and J. L. M. Rupp, *ACS Appl. Energy Mater.*, 2020, **3**, 4569–4579.
- 59 C. Tang, K. Kousi, D. Neagu and I. S. Metcalfe, *Chem. – Eur. J.*, 2021, **27**, 6666–6675.
- 60 O. Kwon, K. Kim, S. Joo, H. Y. Jeong, J. Shin, J. W. Han, S. Sengodan and G. Kim, *J. Mater. Chem. A*, 2018, **6**, 15947–15953.
- 61 S. Jo, Y. Han Kim, H. Jeong, C. Ho Park, B.-R. R. Won, H. Jeon, K. Taek Lee and J. Ha Myung, *Appl. Energy*, 2022, **323**, 119615.
- 62 M. Qin, Y. Xiao, H. Yang, T. Tan, Z. Wang, X. Fan and C. Yang, *Appl. Catal., B*, 2021, **299**, 120613.
- 63 E. I. Papaioannou, D. Neagu, W. K. W. Ramli, J. T. S. Irvine and I. S. Metcalfe, *Top. Catal.*, 2019, **62**, 1149–1156.
- 64 D. Papargyriou, D. N. Miller and J. T. S. Irvine, *J. Mater. Chem. A*, 2019, **7**, 15812–15822.
- 65 A. J. Carrillo and J. M. Serra, *Catalysts*, 2021, **11**, 741.
- 66 S. Joo, A. Seong, O. Kwon, K. Kim, J. H. Lee, R. J. Gorte, J. M. Vohs, J. W. Han and G. Kim, *Sci. Adv.*, 2020, **6**, 1–9.
- 67 H. M. Ansari, A. S. Bass, N. Ahmad and V. I. Birss, *J. Mater. Chem. A*, 2022, **10**, 2280–2294.
- 68 X. Meng, Y. Wang, Y. Zhao, T. Zhang, N. Yu, X. Chen, M. Miao and T. Liu, *Electrochim. Acta*, 2020, **348**, 136351.
- 69 H. Lv, L. Lin, X. Zhang, D. Gao, Y. Song, Y. Zhou, Q. Liu, G. Wang and X. Bao, *J. Mater. Chem. A*, 2019, **7**, 11967–11975.
- 70 Y. Wang, T. Liu, M. Li, C. Xia, B. Zhou and F. Chen, *J. Mater. Chem. A*, 2016, **4**, 14163–14169.
- 71 J. Xu, M. Wu, Z. Song, Y. Chen, L. Zhang, L. Wang, H. Cai, X. Su, X. Han, S. Wang and W. Long, *J. Eur. Ceram. Soc.*, 2021, **41**, 4537–4551.
- 72 P. B. Managutti, S. Tymen, X. Liu, O. Hernandez, C. Prestipino, A. Le Gal La Salle, S. Paul, L. Jalowiecki-Duhamel, V. Dorcet,



- A. Billard, P. Briois and M. Bahout, *ACS Appl. Mater. Interfaces*, 2021, **13**, 35719–35728.
- 73 Z. Du, Y. Gong, H. Zhao, Y. Zhang, S. Yi and L. Gu, *ACS Appl. Mater. Interfaces*, 2021, **13**, 3287–3294.
- 74 C. Solís, M. Balaguer, F. Bozza, N. Bonanos and J. M. Serra, *Appl. Catal., B*, 2014, **147**, 203–207.
- 75 S. Liu, K. T. Chuang and J. L. Luo, *ACS Catal.*, 2016, **6**, 760–768.
- 76 H. Lv, L. Lin, X. Zhang, Y. Song, H. Matsumoto, C. Zeng, N. Ta, W. Liu, D. Gao, G. Wang and X. Bao, *Adv. Mater.*, 2020, **32**, 1906193.
- 77 H. Lv, L. Lin, X. Zhang, R. Li, Y. Song, H. Matsumoto, N. Ta, C. Zeng, Q. Fu, G. Wang and X. Bao, *Nat. Commun.*, 2021, **12**, 5665.
- 78 J. Guo, R. Cai, E. Cali, G. E. Wilson, G. Kerherve, S. J. Haigh and S. J. Skinner, *Small*, 2022, **18**, 1–10.
- 79 S. Joo, K. Kim, O. Kwon, J. Oh, H. J. Kim, L. Zhang, J. Zhou, J. Wang, H. Y. Jeong, J. W. Han and G. Kim, *Angew. Chem., Int. Ed.*, 2021, 19104.
- 80 M. Santaya, H. E. Troiani, A. Caneiro and L. V. Moggi, *ACS Appl. Energy Mater.*, 2020, **3**, 9528–9533.
- 81 T. Chen, S. Sun, Y. He, H. Leng, C. Sun and C. Wu, *J. Alloys Compd.*, 2023, **960**, 170974.
- 82 Y. Jiang, Y. Yang, C. Xia and H. J. M. Bouwmeester, *J. Mater. Chem. A*, 2019, **7**, 22939–22949.
- 83 Q. Liu, D. E. Bugaris, G. Xiao, M. Chmara, S. Ma, H. C. Zur Loye, M. D. Amiridis and F. Chen, *J. Power Sources*, 2011, **196**, 9148–9153.
- 84 Q. Liu, X. Dong, G. Xiao, F. Zhao and F. Chen, *Adv. Mater.*, 2010, **22**, 5478–5482.
- 85 S. Hou, X. Ma, Y. Shu, J. Bao, Q. Zhang, M. Chen, P. Zhang and S. Dai, *Nat. Commun.*, 2021, **12**, 5917.
- 86 M. Najimu, S. Jo and K. L. Gilliard-AbdulAziz, *Acc. Chem. Res.*, 2023, **56**, 3132–3141.
- 87 A. Nanning and J. Fleig, *Surf. Sci.*, 2019, **680**, 43–51.
- 88 L. Chen, J. Xu, X. Wang and K. Xie, *Int. J. Hydrogen Energy*, 2020, **45**, 11901–11907.
- 89 T. Tan, Z. Wang, M. Qin, W. Zhong, J. Hu, C. Yang and M. Liu, *Adv. Funct. Mater.*, 2022, **32**, 2202878.
- 90 F. Fang, N. Feng, P. Zhao, C. Chen, X. Li, J. Meng, G. Liu, L. Chen, H. Wan and G. Guan, *Chem. Eng. J.*, 2019, **372**, 752–764.
- 91 J. H. Kim, S. Yoo, R. Murphy, Y. Chen, Y. Ding, K. Pei, B. Zhao, G. Kim, Y. Choi and M. Liu, *Energy Environ. Sci.*, 2021, **14**, 1506–1516.
- 92 C. Duan, R. Kee, H. Zhu, N. Sullivan, L. Zhu, L. Bian, D. Jennings and R. O'Hayre, *Nat. Energy*, 2019, **4**, 230–240.
- 93 D. S. Tsvetkov, I. L. Ivanov, D. A. Malyshekin and A. Y. Zuev, *J. Mater. Chem. A*, 2016, **4**, 1962–1969.
- 94 R. Strandbakke, V. A. Cherepanov, A. Y. Zuev, D. S. Tsvetkov, C. Argiris, G. Sourkouni, S. Prünste and T. Norby, *Solid State Ionics*, 2015, **278**, 120–132.
- 95 I. Szpunar, R. Strandbakke, M. H. Sørby, S. L. Wachowski, M. Balaguer, M. Tarach, J. M. Serra, A. Witkowska, E. Dzik, T. Norby, M. Gazda and A. Mielewczyk-Gryń, *Materials*, 2020, **13**, 1–18.
- 96 S. L. Wachowski, I. Szpunar, M. H. Sørby, A. Mielewczyk-Gryń, M. Balaguer, C. Ghica, M. C. Istrate, M. Gazda, A. E. Gunnæs, J. M. Serra, T. Norby and R. Strandbakke, *Acta Mater.*, 2020, **199**, 297–310.
- 97 Y. Zhou, E. Liu, Y. Chen, Y. Liu, L. Zhang, W. Zhang, Z. Luo, N. Kane, B. Zhao, L. Soule, Y. Niu, Y. Ding, H. Ding, D. Ding and M. Liu, *ACS Energy Lett.*, 2021, **6**, 1511–1520.
- 98 Y. Niu, Y. Zhou, W. Zhang, Y. Zhang, C. Evans, Z. Luo, N. Kane, Y. Ding, Y. Chen, X. Guo, W. Lv and M. Liu, *Adv. Energy Mater.*, 2022, **12**, 1–9.
- 99 K. Park, M. Saqib, H. Lee, D. Shin, M. Jo, K. M. Park, M. Hamayun, S. H. Kim, S. Kim, K. Lee, R. O'Hayre, M. Choi, S.-J. Song and J.-Y. Park, *Energy Environ. Sci.*, 2024, **17**, 1175–1188.
- 100 P. K. Dubey, J. Hong, M. R. Anisur, K. Lee, S. Belko and P. Singh, *ACS Appl. Energy Mater.*, 2023, **6**, 657–666.
- 101 Y.-F. Sun, Y.-L. Yang, J. Chen, M. Li, Y.-Q. Zhang, J.-H. Li, B. Hua and J.-L. Luo, *Chem. Commun.*, 2018, **54**, 1505–1508.
- 102 D. Merki and X. Hu, *Energy Environ. Sci.*, 2011, **4**, 3878–3888.
- 103 Y. Q. Zhang, H. B. Tao, Z. Chen, M. Li, Y. F. Sun, B. Hua and J. L. Luo, *J. Mater. Chem. A*, 2019, **7**, 26607–26617.
- 104 A. K. Opitz, A. Nanning, V. Vonk, S. Volkov, F. Bertram, H. Summerer, S. Schwarz, A. Steiger-Thirnsfeld, J. Bernardi, A. Stierle and J. Fleig, *Nat. Commun.*, 2020, **11**, 1–10.
- 105 H. Summerer, A. Nanning, C. Rameshan and A. K. Opitz, *EES Catal.*, 2023, **1**, 274–289.
- 106 Y. Lu, Y. Huang, Z. Xu, K. Yang, W. Bao and Q. Lu, *ACS Nano*, 2023, **17**, 14005–14013.
- 107 M. Xu, R. Cao, S. Wu, J. G. Lee, D. Chen and J. T. S. Irvine, *J. Mater. Chem. A*, 2023, **11**, 13007–13015.
- 108 J. Kim, S. Gunduz, A. C. Co and U. S. Ozkan, *Appl. Catal., B*, 2024, **344**, 123603.
- 109 W. Fan, B. Wang, R. Gao, G. Dimitrakopoulos, J. Wang, X. Xiao, L. Ma, K. Wu, B. Yildiz and J. Li, *J. Am. Chem. Soc.*, 2022, **144**, 7657–7666.
- 110 H. Khalid, A. ul Haq, B. Alessi, J. Wu, C. D. Savaniu, K. Kousi, I. S. Metcalfe, S. C. Parker, J. T. S. Irvine, P. Maguire, E. I. Papaioannou and D. Mariotti, *Adv. Energy Mater.*, 2022, **12**, 2201131.
- 111 E. Shin, D. H. Kim, J. H. Cha, S. Yun, H. Shin, J. Ahn, J. S. Jang, J. W. Baek, C. Park, J. Ko, S. Park, S. Y. Choi and I. D. Kim, *ACS Nano*, 2022, **16**, 18133–18142.
- 112 X. Hu, J. Qi, S. Qiao, W. Yu, J. Shang, L. Liu, Z. Zhao, L. Tang and W. Zhang, *Nanotechnology*, 2023, **34**, 105709.
- 113 J. Wang, K. B. Woller, A. Kumar, Z. Zhang, H. Zhou, I. Waluyo, A. Hunt, J. M. LeBeau and B. Yildiz, *Energy Environ. Sci.*, 2023, **16**, 5464–5478.
- 114 M. B. Katz, G. W. Graham, Y. Duan, H. Liu, C. Adamo, D. G. Schlom and X. Pan, *J. Am. Chem. Soc.*, 2011, **133**, 18090–18093.
- 115 M. B. Katz, S. Zhang, Y. Duan, H. Wang, M. Fang, K. Zhang, B. Li, G. W. Graham and X. Pan, *J. Catal.*, 2012, **293**, 145–148.
- 116 H. Han, Y. Xing, B. Park, D. I. Bazhanov, Y. Jin, J. T. S. Irvine, J. Lee and S. H. Oh, *Nat. Commun.*, 2022, **13**, 6682.
- 117 S. J. Kim, T. Akbay, J. Matsuda, A. Takagaki and T. Ishihara, *ACS Appl. Energy Mater.*, 2019, **2**, 1210–1220.
- 118 J. Hyodo, K. Tominaga, S. Ida and T. Ishihara, *J. Mater. Chem. A*, 2016, **4**, 3844–3849.
- 119 M. L. Weber, B. Šmíd, U. Breuer, M.-A. Rose, N. H. Menzler, R. Dittmann, R. Waser, O. Guillon, F. Gunkel and C. Lenser, *Nat. Mater.*, 2024, 1–26.
- 120 M. L. Weber, M. Wilhelm, L. Jin, U. Breuer, R. Dittmann, R. Waser, O. Guillon, C. Lenser and F. Gunkel, *ACS Nano*, 2021, **15**, 4546–4560.
- 121 H. Guo, C. Mead, M. Balingit, S. Shah, X. Wang, M. Xu, I. Tran, T. Aoki, J. D. Samaniego, K. L. Gilliard-AbdulAziz, L. J. Lauhon and W. J. Bowman, *Matter*, 2024, **7**, 1002–1017.
- 122 M. Melchionna and P. Fornasiero, *RSC Appl. Interfaces*, 2024, **1**, 70–79.
- 123 C. Bozo, N. Guillaume and J. M. Herrmann, *J. Catal.*, 2001, **203**, 393–406.
- 124 M. Balaguer, C. Solís and J. M. Serra, *J. Phys. Chem. C*, 2012, **116**, 7975–7982.
- 125 M. Laqdiem, A. J. Carrillo, G. Dimitrakopoulos, M. Balaguer, J. Garcia-Fayos, A. F. Ghoniem and J. M. Serra, *Solid State Ionics*, 2023, **394**, 116192.
- 126 M. A. Naeem, P. M. Abdala, A. Armutlulu, S. M. Kim, A. Fedorov and C. R. Müller, *ACS Catal.*, 2020, **10**, 1923–1937.
- 127 Y. Xiao and K. Xie, *Angew. Chem., Int. Ed.*, 2022, **61**, 1–8.
- 128 K. Wu, J. Matsuda, A. Staykov and T. Ishihara, *Adv. Energy Mater.*, 2023, **13**, 1–16.
- 129 F. Hu, K. Chen, Y. Ling, Y. Huang, S. Zhao, S. Wang, L. Gui, B. He and L. Zhao, *Adv. Sci.*, 2023, **2306845**, 1–11.
- 130 M. Kim, G. Kwon, W.-G. Jung, Y. Choi, B.-J. Kim and H. Lee, *ACS Appl. Mater. Interfaces*, 2021, **13**, 48508–48515.
- 131 S. Joo, C. Lim, O. Kwon, L. Zhang, J. Zhou, J.-Q. Wang, H. Y. Jeong, Y. Sin, S. Choi and G. Kim, *Mater. Rep.: Energy*, 2021, 100021.
- 132 W. Yang, X. Wang, S. Song and H. Zhang, *Chem*, 2019, **5**, 1743–1774.
- 133 W. Qi, K. Xie, M. Liu, G. Wu, Y. Wang, Y. Zhang and Y. Wu, *RSC Adv.*, 2014, **4**, 40494–40504.
- 134 J. Tan, D. Lee, J. Ahn, B. Kim, J. Kim and J. Moon, *J. Mater. Chem. A*, 2018, **6**, 18133–18142.
- 135 J. Lee, M. Bae and J. Bae, *Int. J. Hydrogen Energy*, 2022, **47**, 29327–29336.



- 136 J. Lee, C. Yeon, J. Oh, G. Han, J. Do Yoo, H. J. Yun, C. W. Lee, K. T. Lee and J. Bae, *Appl. Catal., B*, 2022, **316**, 121645.
- 137 L. Z. Gan, L. T. Ye, C. Ruan, S. G. Chen and K. Xie, *Adv. Sci.*, 2015, **3**, 1–7.
- 138 M. L. Weber, D. Jennings, S. Fearn, A. Cavallaro, M. Prochazka, A. Gutsche, L. Heymann, J. Guo, L. Yasin, S. J. Cooper, J. Mayer, W. Rheinheimer, R. Dittmann, R. Waser, O. Guillon, C. Lenser, S. J. Skinner, A. Aguadero, S. Nemsák and F. Gunkel, *ChemRxiv*, 2023, preprint, DOI: [10.26434/chemrxiv-2023-8k11w](https://doi.org/10.26434/chemrxiv-2023-8k11w).
- 139 S. Kang, J. K. Kim, H. Kim, Y. Son, J. Chang, J. Kim, D. Kim, J. Lee and H. J. Kwon, *Nano Lett.*, 2024, **24**, 4224–4232.

